Temporal Change of Seismic Velocity and Site Response for Different Scales and Implications for Nonlinearity

A Thesis
Presented to
The Academic Faculty

By

Chunquan Wu

In Partial Fulfillment
Of the Requirements for the Degree
Master of Science in Earth and Atmospheric Sciences

Georgia Institute of Technology

August, 2007

Temporal Change of Seismic Velocity and Site Response for Different Scales and Implications for Nonlinearity

Approved by:

Dr. Zhigang Peng, Advisor
School of Earth and Atmospheric Sciences
Georgia Institute of Technology

Dr. Leland T. Long
School of Earth and Atmospheric Sciences
Georgia Institute of Technology

Dr. Andrew V. Newman
School of Earth and Atmospheric Sciences
Georgia Institute of Technology

Date Approved: July 6, 2007

ACKNOWLEDGEMENTS

I would like to thank my advisor Dr. Zhigang Peng for his aborative and patient guidance throughout the study. I am thankful to Dr. Tim Long, my previous advisor, for his insightful suggestions and help in the first part of this study. I am also thankful to Dr. Andrew V. Newman for taking the time to serve on my thesis committee. Special thanks to Dr. Tatiana D. Toteva for her help in the field data collection and Susan Ryan for her carefully grammar checking of my thesis. I would also like to thank all the other colleagues in the geophysics program in the school of Earth and Atmospheric Sciences, Georgia Tech for their help and support.

I would like to express my gratitude to my parents and friends, for their enduring support and encouragement.

TABLE OF CONTENTS

LIST OF TABLES

LIST OF FIGURES

SUMMARY

This thesis consists of two major parts. In the first part, I monitor the temporal change of *S*-wave velocity in shallow soil layers using seismic data collected in an experiment at Panola Mt. Atlanta, GA, 2006. I use the cross-correlation function to find the arrival time differences for different water levels, and then calculate the change of Rayleigh wave phase velocity according to different frequencies in the range 5 to 50 Hz. After that, I find a reference 1-D layered *P* and *S*-wave velocity model from the measured Rayleigh wave dispersion curve, and put 6 sets of Gaussian perturbations into the reference velocity structure to invert for the actual temporal change of velocity structure in the experiment. I find a clear increase of *S*-wave velocity in the water injection area, and the *S*-wave velocity gradually recovers to the initial value after we stop pumping water.

In the second part, I analyze temporal changes in fault zone site response along the Karadere-Düzce branch of the North Anatolian Fault, starting 8 days before and ending 72 days after the 1999 Mw7.1 Düzce, Turkey, earthquake. The analysis involves comparisons of strong motion seismic records at station VO inside the Karadere fault and station FP about 300 m away from the fault. I compare all available seismic waveforms at these stations, including those generated by foreshocks, the mainshock, aftershocks and seismic noise, and cut them into 10 s windows with a 5 s overlap. Fourier amplitude spectra are computed for seismic data in each window, and the average amplitude spectra for the two horizontal components

are used to obtain the spectral ratio for each on/off fault pair of seismic records. The spectral ratios are smoothed over every 10 points in the frequency domain (0.5 Hz). The results show a shift of the spectral peak to lower frequencies during the main shock. The peak frequency reduces from 4.3 Hz several days before the main shock to 2.9 Hz (67.4% of the pre mainshock value) right after the mainshock. It quickly recovers to 3.8 Hz (64% recovery of the dropped value) after a day, and then gradually recovers to 4.0 Hz (79% recovery of the dropped value) after 72 days. I also compare the results from all the seismic data including direct *S*-wave, *S* coda waves and seismic noise and from coda waves only and find that the results from coda waves which are generally less scattered than those from all the data, and show lower amplitude of spectra ratio with higher peak frequencies. The observations suggest a nonlinear behavior of the fault zone material under strong ground motion of nearby major earthquakes.

Finally I attempt to link the two parts by identifying their implications for the nonlinear site effects.

CHAPTER 1

INTRODUCTION

Almost everybody's childhood memories include something to do with colorful balloons, including mine. Imagine thousands of balloons with shining flowery colors rising under the clear blue sky. What a beautiful scene it is. However the rising balloons would finally blow up due to the decreasing air pressure or other excitations high in the sky. That is why many writers and artists use balloons in their work as a symbol of human beings' fragile dreams, and the blowing up of balloons as the final realization that many initial wishes are just cloud-castles after passion fades as time moves on.

However, scientists and engineers look at things in different ways than writers and artists. The distinct behavior of balloons under different levels of pressure can illustrate nonlinearity in our everyday lives. When you press a balloon with both of your hands gently, its shape changes a little. After you release your hands, it recovers to the original shape. This is a linear portion of its response to stress. But what would happen if you press the balloon with all your strength in your hands, very, very harshly? It would finally rupture and never recover to its initial status. This phenomenon is an example for material behavior before and after the loading exceeding its linear range, although the analogy is not exact. For that reason, we have to first look at the definitions of linearity and nonlinearity.

1.1 Definition of Linearity and Nonlinearity

The word linear comes from the Latin word *linearis*, which means "created by lines." In mathematics, a linear function $f(x)$ is one which satisfies the following two properties: (1) additivity property (also called the superposition property) $f(x+y) = f(x) + f(y)$, which means f is a group homomorphism with respect to addition; (2) homogeneity property: $f(ax) = af(x)$ for all a. It turns out that homogeneity follows the additivity property in all cases where a is rational. In that case if $f(x)$ is continuous, homogeneity is not an additional axiom to establish if the additivity property is established. In comparison, the behavior of the nonlinear systems can not be expressed as a sum of the behaviors of its descriptors. In particular, they are not subject to the principle of superposition as linear systems are.

In the case of a balloon, if we plot the stress-strain relationship before it bursts, the relation could be approximate as a straight line, indicating linearly elastic strain increase. However, as the stress exceeds its yield strength, the balloon is permanently distorted and eventually ruptures. Beyond the yield strength, strain begins to change nonlinearly, and eventually ruptures. Instead of continuing to increase linearly with stress it bursts. Scientists use linear models to describe the behavior of most systems in nature. However, it is important to know that there are almost no perfectly linear systems in the physical world. The so-called linear systems in physics are usually quasi-linear systems in which the nonlinear effects in the system are not significant enough to affect the overall linear property of the system. In addition, nonlinear

systems are more difficult to understand because their solutions are more complex due to their lack of simple superposed solutions. For instance, our Earth is an elastic and fluid gravitating ellipsoid on a large scale. But when we go to smaller scales, many materials and structures at the surface and inside the Earth have nonlinear behaviors. I will present some examples in the following sections.

1.2 Nonlinear Effects in Geophysics

A well-known example of nonlinear effects in geophysics is the nonlinearity response of soil to applied stress. Geotechnical engineers have recognized for decades that the stress-strain behavior of soils in the laboratory is nonlinear. Many experimental studies since the 1970s (e.g., Seed and Idriss, 1970; Hardin and Drnevich, 1972a, b) have investigated the nonlinear effects on soil properties over a wide range of strain. These empirical results are widely used in engineering design to model the nonlinearity of soil.

On the other hand, seismologists generally use linear models of elastic response of the Earth to model teleseismic waves as well as strong ground motions. One example for this is the successful utilization of empirical Green's functions, or the weak motions generated by small earthquakes, to predict strong ground motion (e.g., Hartzel, 1978; Kanamori, 1979; Hadley and Helmberger, 1980; Tanaka et al., 1982; Irikura, 1983; Munguia and Bruna, 1984; Aki and Irikura, 1991). As stated in a review paper (Aki, 1988), many studies have shown that the site effects on weak

motions are consistent with those under strong motions (e.g., Borcherdt, 1970, 1990; Murphy et al., 1971; Joyner et al., 1981; Rogers et al., 1984, 1985; Tucker and King, 1984; Kobayashi and Midorikewa, 1986; Singh et al., 1988; Jongmans and Campillo, 1990). However, there is growing evidence that nonlinear amplification of strong ground motion does occur in soil sites (e.g., Boore et al., 1989; Chin and Aki, 1991; Darragh and Shakal, 1991a, b). This controversy on whether nonlinear model is necessary is increasing seismological interests in nonlinear site effects.

1.3 Seismological Study of Nonlinear Effects

Nonlinear site effects are the result of change in site property after strong motion or other large amplitude excitations. The energy may be shifted to different frequencies, hence the spectral amplitudes for the output are not always in proportion to the input frequency amplitude. Monitoring the temporal change in the site response is the typical way to examine the source of nonlinear effects. Because seismic velocity is sensitive to both the structure and the material property, such as elastic modulus, it is an effective measure of the system property in both large and small scales. Many researchers have successfully used temporal changes in seismic velocity to find evidence for nonlinearity (e.g., Poupinet et al., 1984; Ozalaybey et al., 1997; Aguirre and Irikura, 1997; West and Menke, 2001; Schaff and Beroza, 2004; Rubinstein and Beroza, 2004; Peng and Ben-Zion, 2006; Rubinstein et al., 2007).

Another way to test for the effects of nonlinearity is to measure the Fourier or

response spectral ratio between two nearby stations in a study area. The spectral ratio of two receivers gives a direct indication of the site response between them. Many seismologists use this method to examine the soil nonlinearity by taking the response spectral ratio between rock and soil surface motions (Jarpe et al., 1988, 1989; Seed 1988; Chang et al., 1990; Darragh and Shakal, 1991a, 1991b; Archuleta et al., 1992; Wen, 1994; Wen, et al. 1994, 1995; Beresnev et al., 1995a, 1995b; Wen and Beresnev, 1996; Field et al., 1997; Higashi and Sasatani, 2000; Yalcinkaya and Alptekin, 2005), and their results generally show two effects: attenuation of strong motion and decrease of effective frequency of waves in the soil. Both of these effects are consistent with the geotechnical laboratory results.

In recent years, the usage of spectral ratio method has expanded beyond the comparison between soil and hard rocks, and now include considerations of the response spectra change between the surface and at the bottom of a borehole array (Sawazaki et al., 2006) and comparison of the response spectra inside and outside the fault zone (Karabulut and Bouchon, 2007). Some of these new studies are focused on the fault zone site response. It is interesting to note their results generally do not follow results expected using traditional soil experiments. This indicates that there could be some differences between soil sample tests in laboratories and the measurements from highly fractured fault zone material in field sites.

Other studies have attempted to examine the nonlinear site effects using the numerical modeling methods, field stress-strain measurements, or combined approaches (e.g., Yu et al., 1993; Schneider et al., 1993; Harmsen, 1997; Beresnev

and Atkinson, 1998; Pavlenko and Irikura, 2003).

Considering all of the studies cited above, the evidence for nonlinear site effects and the model used to describe them are still inconclusive. Because sites vary due to their scales and distinctive properties, and the physical mechanisms for nonlinear site effects are still poorly understood and modeled, the question of whether the nonlinearity is a pervasive or occasional phenomenon remains open. In this thesis, the two methods mentioned above are used to measure temporal change of site properties under physical excitations at different scales. Our results are useful for providing an improved understanding of temporal changes and nonlinear effects in seismology.

CHAPTER 2

TEMPORAL CHANGE OF *S*-WAVE VELOCITY IN SHALLOW LAYERS

2.1 Introduction

Shallow soil layers have long been studied by geotechnical engineers whose research is focused on earthquake induced strong ground motion that is large enough to cause damage on structures on the earth's surface (e.g., Seed and Idriss, 1970; Hardin and Drnevich, 1972a, b). However, only a few studies have focused on temporal changes of seismic velocities in shallow layers due to changes of water table (e.g., Jefferson et al., 1998; Bachrach and Nur, 1998). In these studies it is argued that fluid saturation is one of the most critical factors that have significant influence on the propagation of seismic waves in shallow layers of soil. An experiment on the shallow soil layers of the earth was designed to investigate the temporal change of seismic velocity structure due to change of water table. In the following sections, I will briefly review some basic concepts of seismic wave velocity and previous work. Then I will describe the experiment, data analysis procedure and the results. Finally I will briefly discuss the results and compare them with those from previous studies.

2.1.1 Relationship between Media Properties and Wave Velocities

The wave equations are obtained from the equations of motion, assuming the

infinitesimal stain, homogeneous, isotropic and linear Hooke's law media conditions. Two solutions to the wave equations are the *P*- and *S*-waves with velocities that are related to the media properties by:

$$\alpha = \sqrt{\frac{\lambda + 2\mu}{\rho}} \tag{2.1}$$

$$\beta = \sqrt{\frac{\mu}{\rho}} \tag{2.2}$$

where α is the *P*-wave velocity, β is the *S*-wave velocity, λ and μ are Lame constants, μ is also called shear modulus, and ρ is density.

In the real world, elastic medium is bounded and inhomogeneous. However, a uniform elastic property is generally assumed for its simplicity. Because the change of medium property is the ultimate source of temporal changes in seismic properties, which include changes in seismic velocity, amplification or shift of frequency, it is reasonable to monitor the temporal change of seismic properties to infer changes in material properties.

2.1.2 Previous Work and Motivation

Jefferson et al. (1998) conducted repeated shallow seismic experiments at a site in Lawrence, Kansas, with different near-surface moisture conditions in

unconsolidated material. By keeping all the other experimental field parameters constant, they identified clear correlation between seismic properties and water content within the upper 0.15 m of the subsurface. Bachrach and Nur (1998) conducted high-resolution shallow seismic reflection and refraction experiments at the Moss-Landing Beach in Monterey Bay, California. Their results showed that the near surface velocities in sand are sensitive to partial saturation. Bachrach et al. (1998) conducted another experiment in the same site with investigation depth of about 2 m and found that the lowest velocity for unconsolidated sand could be about 13 m/s, and different geophone interval is necessary to distinguish Rayleigh waves from shallow reflections. Bachrach et al. (2000) determined *P*- and *S*-wave velocity depth profiles in shallow, unconsolidated beach sand by analyzing three-component surface seismic data.

West and Menke (2001) monitored the temporal change of *P*- and *S*-wave velocity structure with water level change induced by tide at a site in East Hampton, New York. They found an increase of *S*-wave velocity in the partially saturated layer with rising water levels (Figure 2.1). Interestingly this result does not follow the relationship between seismic wave velocity and saturation from traditional lab experiments (e.g., Knight and Nolan-Hoeksema, 1990), which states that both *P*- and *S*-wave velocities decrease as moisture is introduced. As maximum saturation is approached, the *P*-wave velocity increases dramatically while the *S*-wave velocity continues to decrease. To explain this, West and Menke (2001) suggested that fluid saturation influence the shear modulus more than the density on the field scale.

Because the shear modulus is significantly increased as water level increases, but the density change is relatively small, the *S*-wave velocity would finally increase according to Equation 2.2.

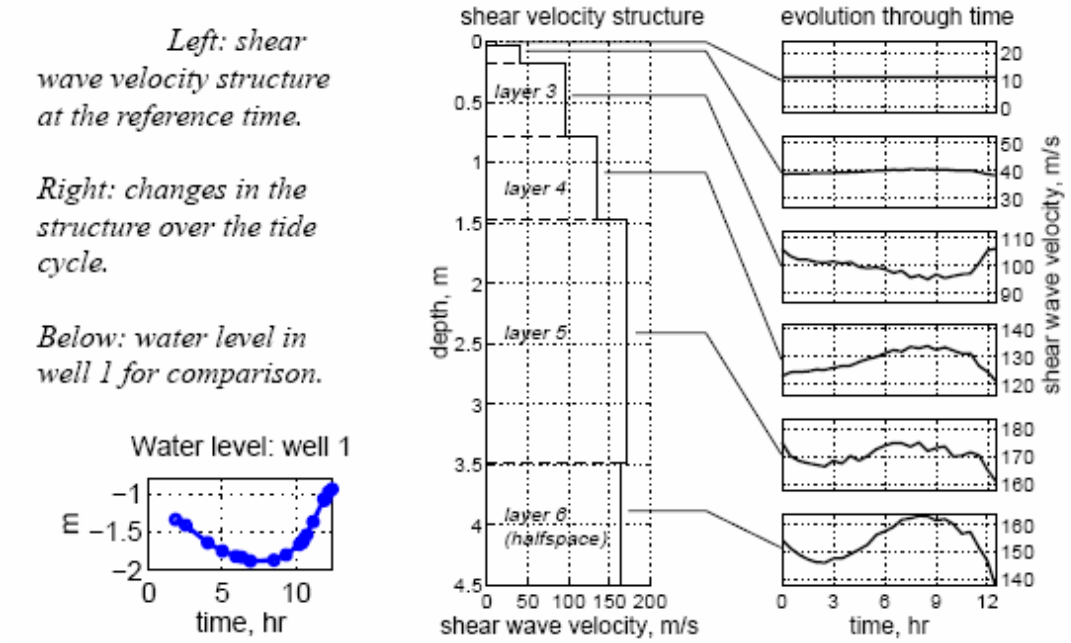

Figure 2.1 Variation of *S*-wave velocity with water level after West and Menke (2001).

Since *S*-wave velocities have potential to be used to monitor temporal change of pressure in a fluid reservoir or other water resources, we design our study following a procedure similar to West and Menke (2001). However, our experiment is carried out in soil rather than near the coast, and our focus is on the shallow soil layers with a much shorter time scale of about 50 minutes than unconsolidated beach sands. Also, the techniques we use for the surface wave analysis and inversion are

quite different.

2.2 Site Information and the Experiment

The experiment reported in this thesis was conducted in the Panola Mountain 20 miles east of Atlanta, Georgia, on March 23, 2006. Figure 2.2 shows the geometry of source, injection point, and receivers. 16 geophones are placed in a straight line with a distance of 1 m between adjacent receivers. The source is also placed in this line with a distance of 6 m from the first receiver. The water injection point is at the midpoint of the 8^{th} and 9^{th} receivers, and depth of water outlet is 3 m underground. The water level is monitored by the electric resistance sensor which is 4.5 m perpendicular from the injection point. Table 2.1 gives the number of shots, the volume of water injected, the state of the well water level monitor, and incidents during the experiment. Figure 2.3 shows the change of water level during the injecting process computed from the resistance reading.

A gravity hammer is used as the seismic source and the hammer is dropped from a constant height to minimize the variations in the source function. 53 shots are generated with a time interval of one minute between two adjacent shots.

Table 2.1 List of shots and the process of water injection.

No. of Shots	Injection Status	Water Level Reading	Incidents
1		1848/856Ω	
2			
3			
4			
5			
6			
7			
8			
9			
10			
11			
12			
13	injection starts after shot		
14	4 Gal of water injection		
15	3 Gal of water injection		
16	4 Gal of water injection		
17	4 Gal of water injection		
18	4 Gal of water injection		
19	4 Gal of water injection		
20	4 Gal of water injection		
21	4 Gal of water injection		
22	end of injection	1892/856Ω	
23			
24			
25			
26			
27			
28			
29			
30			
31			
32		1872/857Ω	
33			noise from ground loop
34			
35			source shorted
36		1866/856Ω	a lizard hits cable of geophone 5
37			
38			
39			

Table 2.1 (continued).

40			laptop battery down, switch to inverter, noise induced
41		1857/856Ω	
42			
43		1848/856Ω	
44			
45			
46			
47			
48			
49			
50			
51			
52			
53			

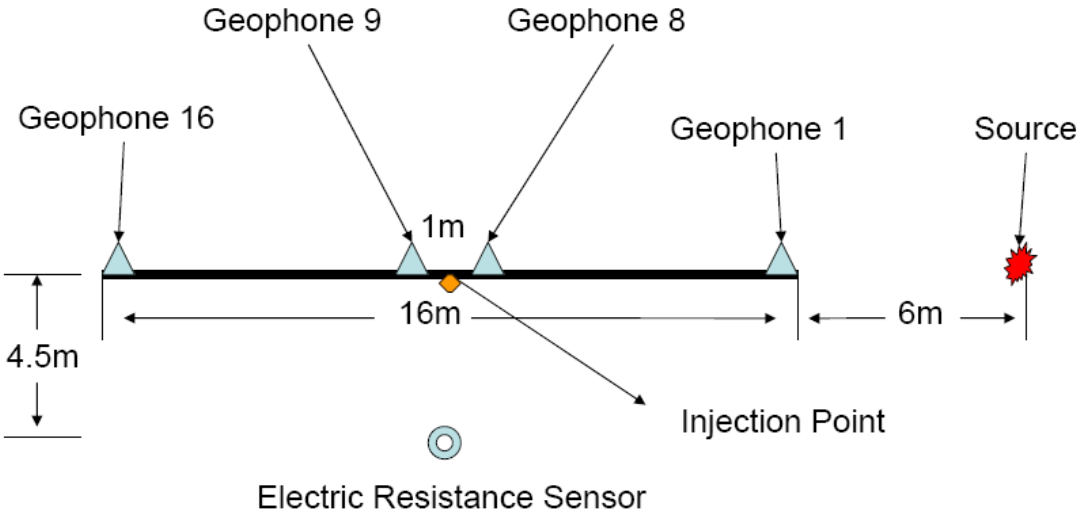

Figure 2.2 Geometry of the experiment. Source is 6 m from the first receiver. Receivers are equally spaced in a line with 1 m interval. Injection point is at the mid-point of the eighth and ninth receivers. Electric resistance sensor is 4.5 m perpendicular to the injection point.

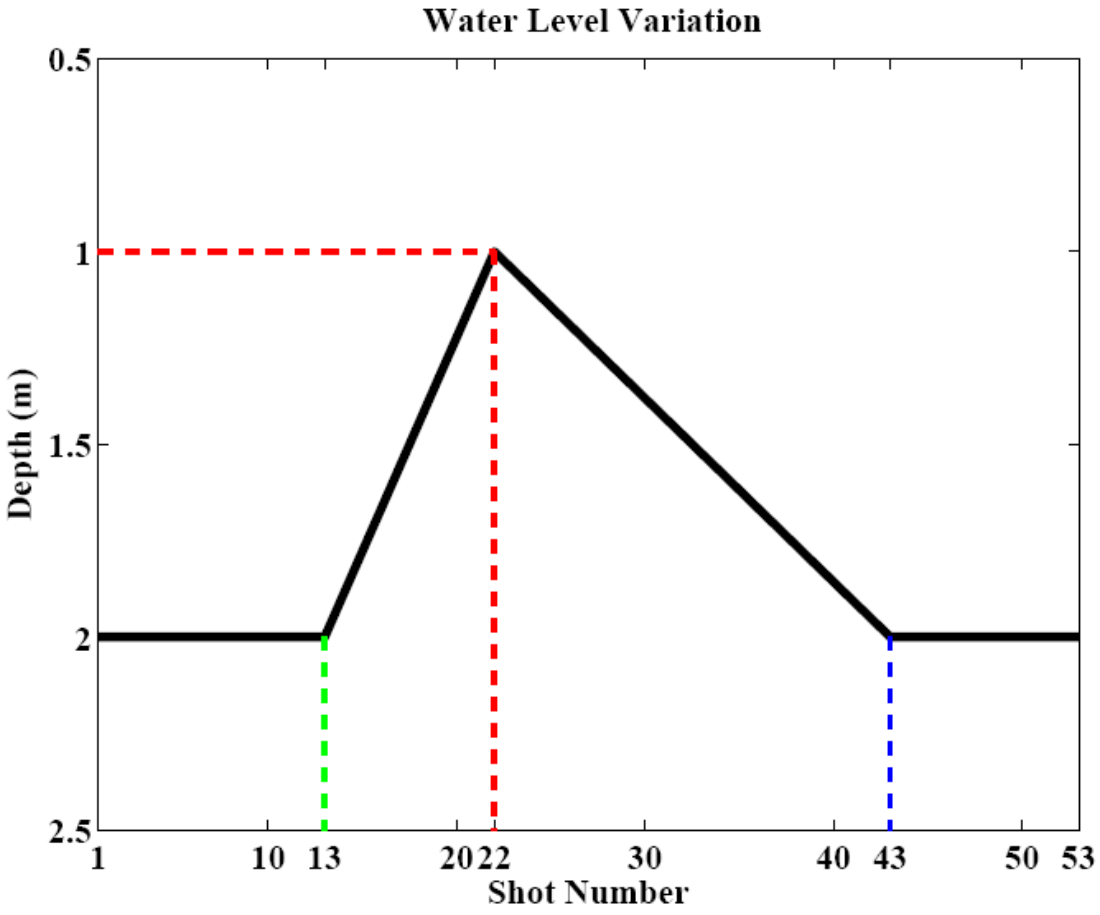

Figure 2.3 Water level variations during the experiment from the resistance water level monitor.

2.3 Seismic Data Preprocessing

The raw data from the experiment includes 848 traces recorded at 16 geophones for 53 shots. Each trace has 4000 data points sampled at time increment of 1.6×10^{-4} s per data point. The first step of preprocessing is to remove the mean value. Sample traces after this step are shown in Figure 2.4 and 2.5. Next, all the traces are aligned by the *P*-wave onset to remove potential origin time errors (Figure 2.6). The *P*-wave onsets of traces from all shots recorded at the first receiver are used as the

reference to measure the origin time correction and then apply this correction to all traces.

Because the source function may also change with time, I also perform a source function correction. To do this, I first select the lowest noise reference shot before injection (the 5th shot) and the lowest noise reference geophone (the 3rd geophone) to find the transfer function (TF) in the frequency domain by taking the spectral ratio,

$$TF = \frac{S_R}{S} \tag{2.3}$$

where S_R is the spectrum of the signal received by the reference geophone for the reference shot, and S is the spectrum of signal received by the reference geophone for all the shots.

This function is used to transform all the other traces from other shots to the reference shot,

$$S_a = S_b \times TF \tag{2.4}$$

where S_a is the spectrum of signal received by all geophones after source function correction, S_b is the spectrum before source function correction.

After this correction, the sources of all the shots can be considered as the same. Data from the last 4 shots are not used because of the low quality, so after the

preprocessing we have 16 (geophones) × 49 (shots) = 784 traces.

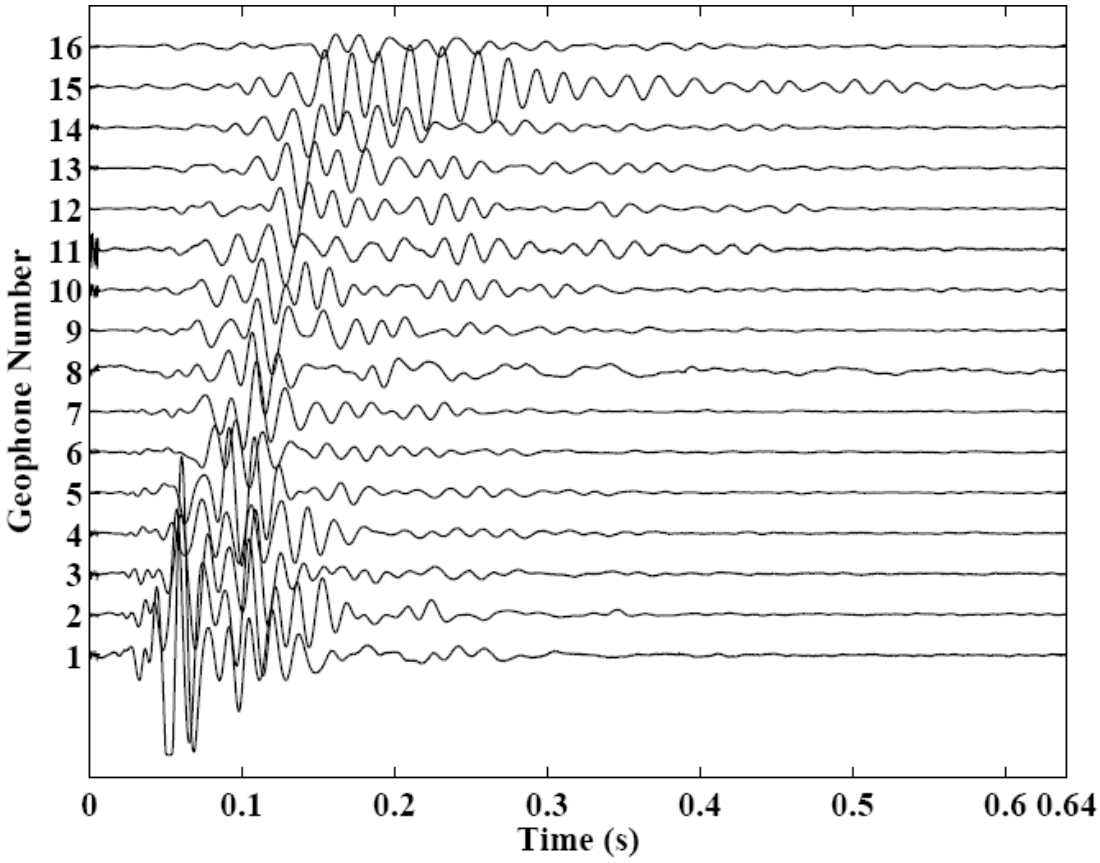

Figure 2.4 Traces from all geophones for shot 16.

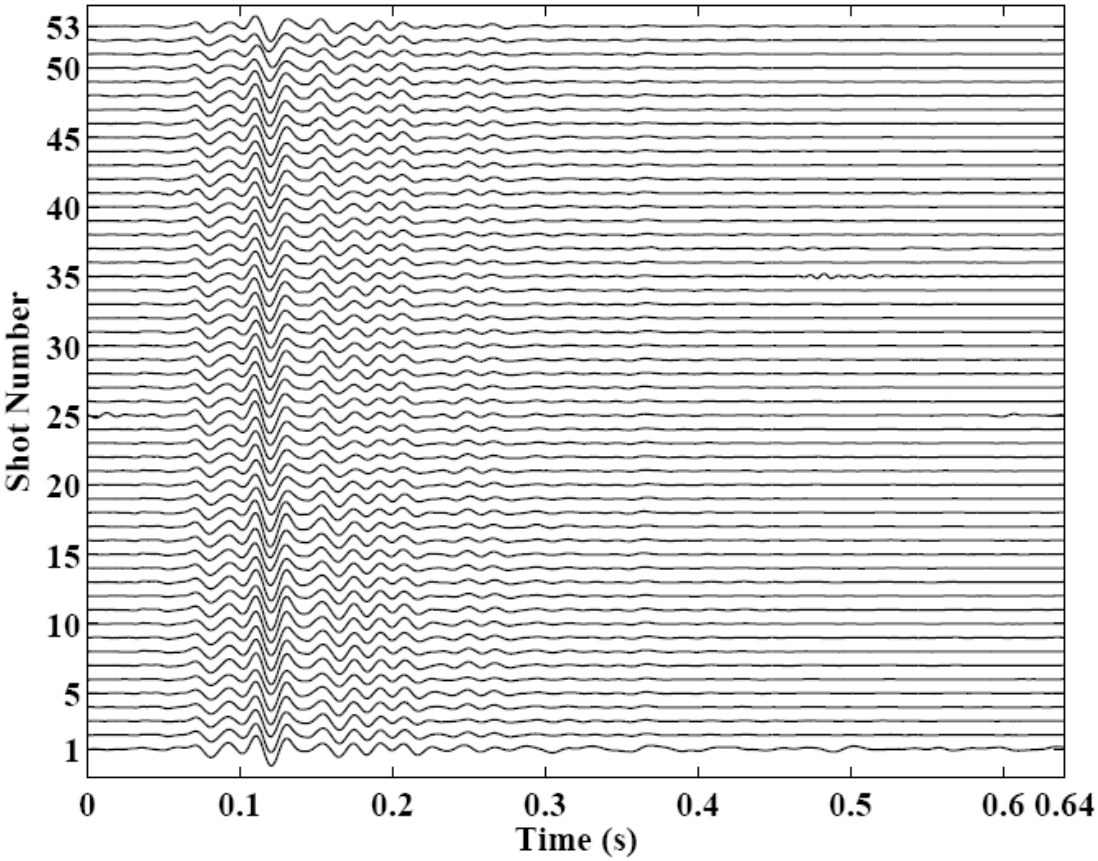

Figure 2.5 Traces of all shots received by geophone 8.

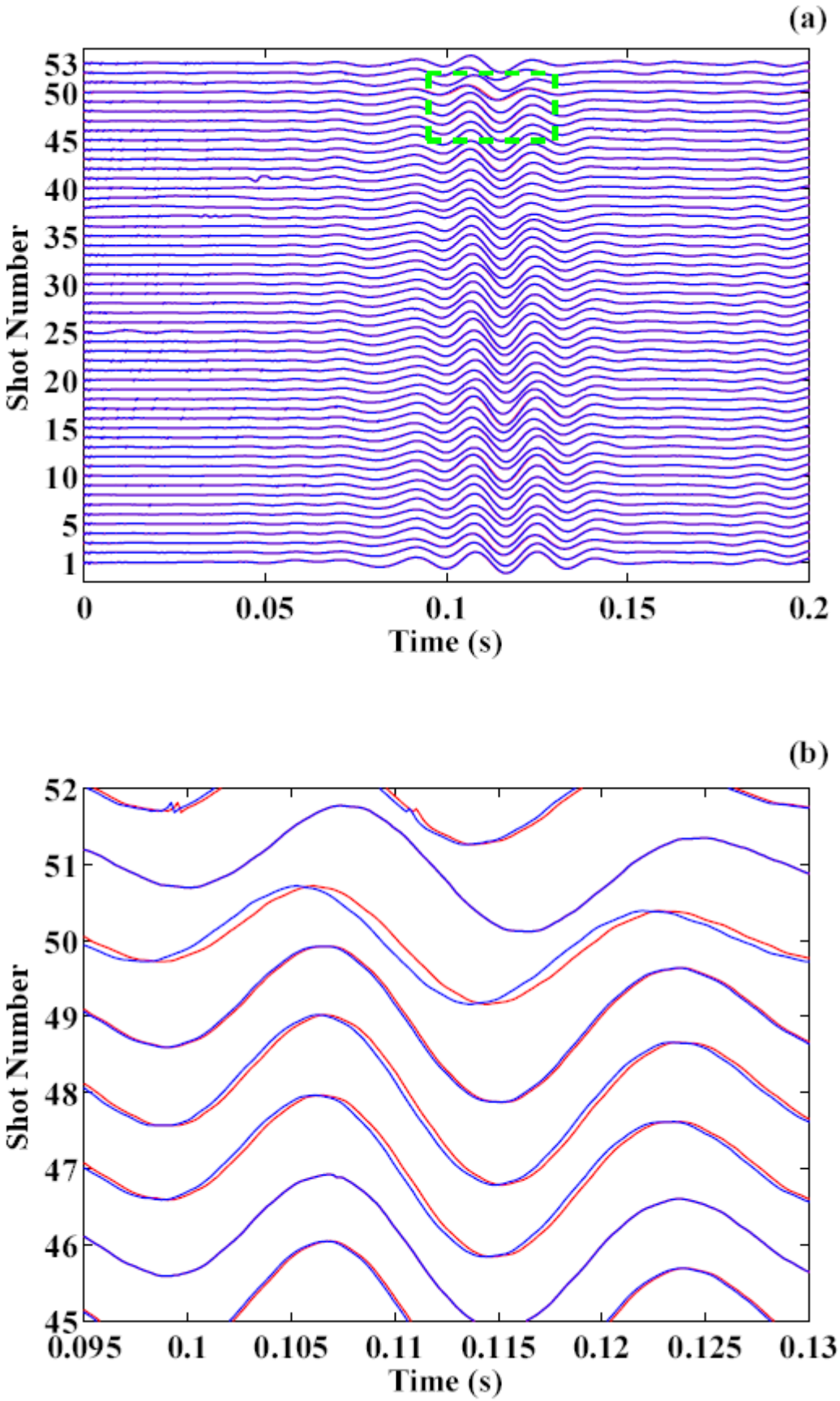

Figure 2.6 (a) Traces of all shots received by geophone 8 before (red) and after (blue)

the origin time correction. The green dashed lines indicate the zoom-in window shown in (b). (b) Detailed view of windowed region in (a) showing some shift of traces after origin time correction.

2.4 Variation in Rayleigh Wave Phase Velocity

2.4.1 Arrival Time Delay Measurement

The traces are dominated by Rayleigh waves (e.g., Figure 2.4 and 2.5). Two approaches are used to find the time differences in Rayleigh waves for different shots. The first approach (in time domain) is to cross correlate all the shots with the first shot and use the peak positions of cross-correlation function to obtain the arrival time differences of Rayleigh waves. The second approach (in frequency domain) is to use FFT (Fast Fourier Transform) to transfer each trace into the frequency domain and calculate the phase of each spectrum. The phase differences in frequency domain provide similar time differences as in time domain. After comparison, I find that the cross-correlation approach in time domain gives more stable and reasonable results, so I apply this approach to measure the arrival time variation of Rayleigh waves. In detail, I first filter the corrected traces with a Gaussian filter with a standard deviation of 5 Hz and center frequencies of 5 to 50 Hz in increments of 5 Hz. The Rayleigh wave arrival time differences are obtained by using the cross-correlation function for each frequency. The arrival time differences for data from geophone 9 filtered at 30 Hz central frequency is shown in Figure 2.7.

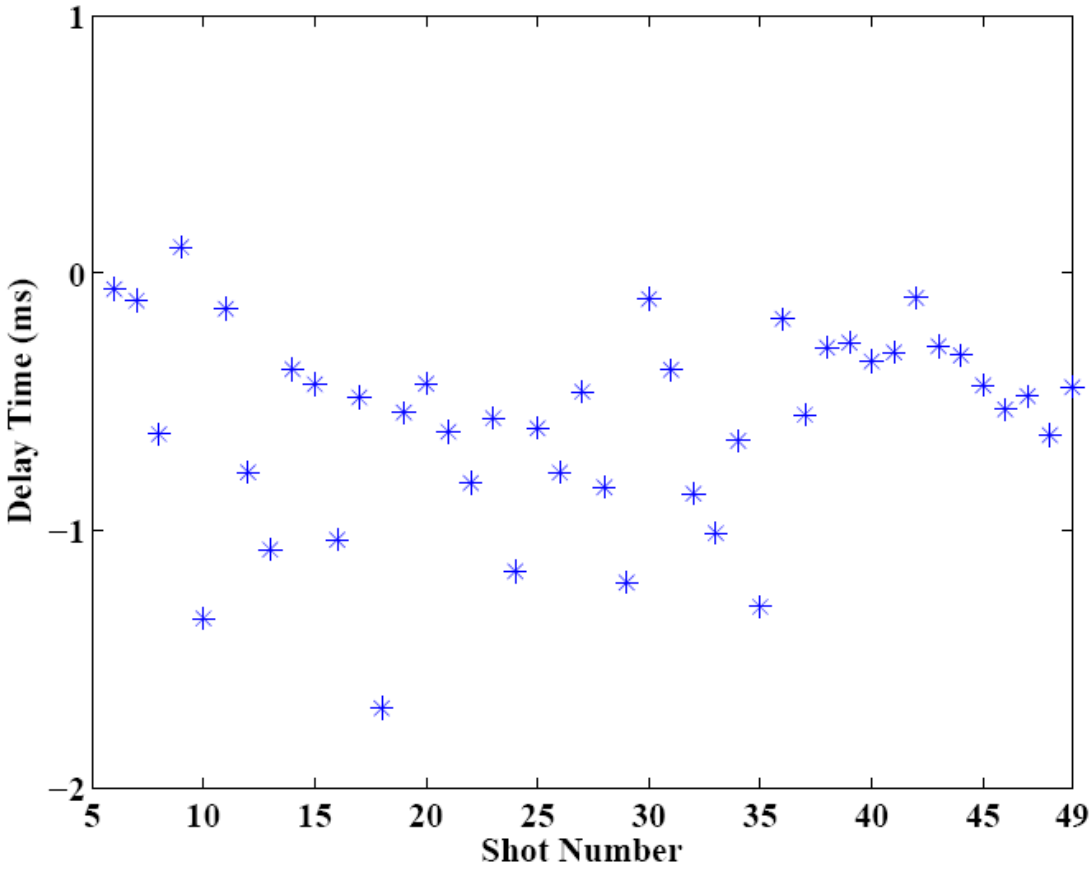

Figure 2.7 Delay time for records from geophone 9 filtered at center frequency of 30 Hz.

2.4.2 Phase Velocity Change from the time delay Measurement

The relationship between time delay Δt and phase velocity change of the Rayleigh wave Δc is

$$\Delta t = \frac{l}{c + \Delta c} - \frac{l}{c} \tag{2.5}$$

where c is phase velocity obtained from the reference phase velocity dispersion curve which is measured using the field data, and l is the horizontal scale of the area

after water injection. Based on comparison of the records from several geophones near the injection region, I found that the injection only influence the records of the 7th geophone and geophones on its left side. Assuming the water flow is isotropic, the value of l is estimated to be 3 m (the distance from 7th to 10th geophone).

Because Δc is much smaller than c, Equation 2.3 can be approximated by ignoring the high-order terms as

$$\Delta c = -\frac{c^2 \times \Delta t}{l} \tag{2.4}$$

2.5 Inversion for the *S*-wave Velocity Structures

2.5.1 Reference Velocity Model and Dispersion Curve

Because the motion of Rayleigh waves can be treated as the combination of *P*- and *S*-wave motions of different phases, the change of Rayleigh wave phase velocity can be traced back to changes of *P*- and *S*-wave velocity structure of the local area. The method of Takeuchi and Saito (1972) is used to calculate the dispersion curve for a one dimensional velocity structure. The input of the program is a 1-D representation of the *P*-wave, *S*-wave and density structure and the output is the dispersion curve of the Rayleigh wave for the given structure. Assuming a $\frac{V_p}{V_s}$ value of $\sqrt{3}$, a reference *P*- and *S*-wave velocity structure is calculated using trial and error from the estimated

dispersion curve. Figure 2.8 shows the estimated Rayleigh wave phase velocity dispersion curve from our field data. The field data are filtered at center frequency of 5 to 50 Hz in increments of 1 Hz. Then for each frequency I identify the arrival time and fit a line, and the slope of the line fitted in the distance versus arrival time plot gives the phase velocity. Figure 2.9 shows the reference seismic wave velocity structure for the studied area interpolated by the program.

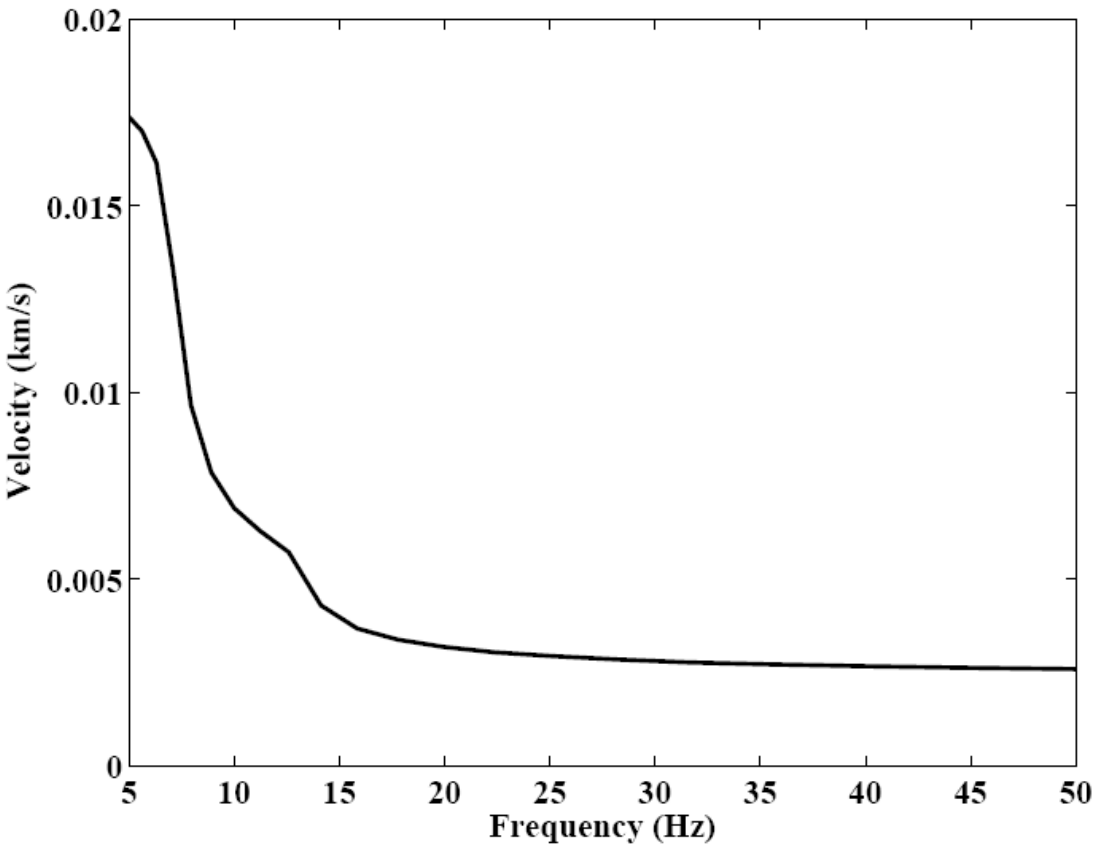

Figure 2.8 Estimated Rayleigh wave phase velocity dispersion curve.

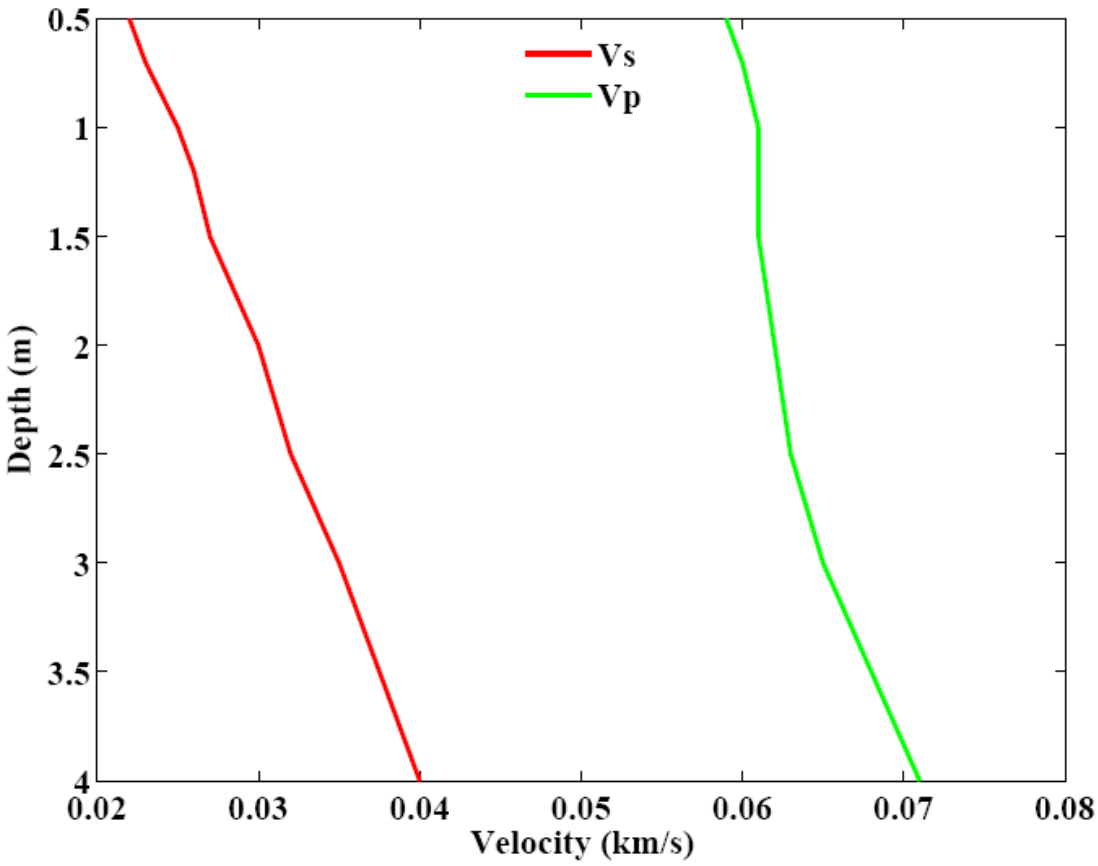

Figure 2.9 Reference *P*- and *S*-wave velocity structure.

2.5.2 Gaussian Function Perturbations

In order to invert phase velocity perturbations as a function of depth, I define six sets of Gaussian function perturbations centered at six different depths of the reference velocity structure and obtain six new velocity structures (Figure 2.10). Using the new velocity structures as the input, six new Rayleigh wave dispersion curves are obtained. After subtracting the reference dispersion curve from these new dispersion curves, I find the changes of phase velocity centered at different frequencies ($[\Delta c_f]$ in matrix form) as the result of perturbations centered at different

depths ($[\Delta V_d]$ in matrix form).

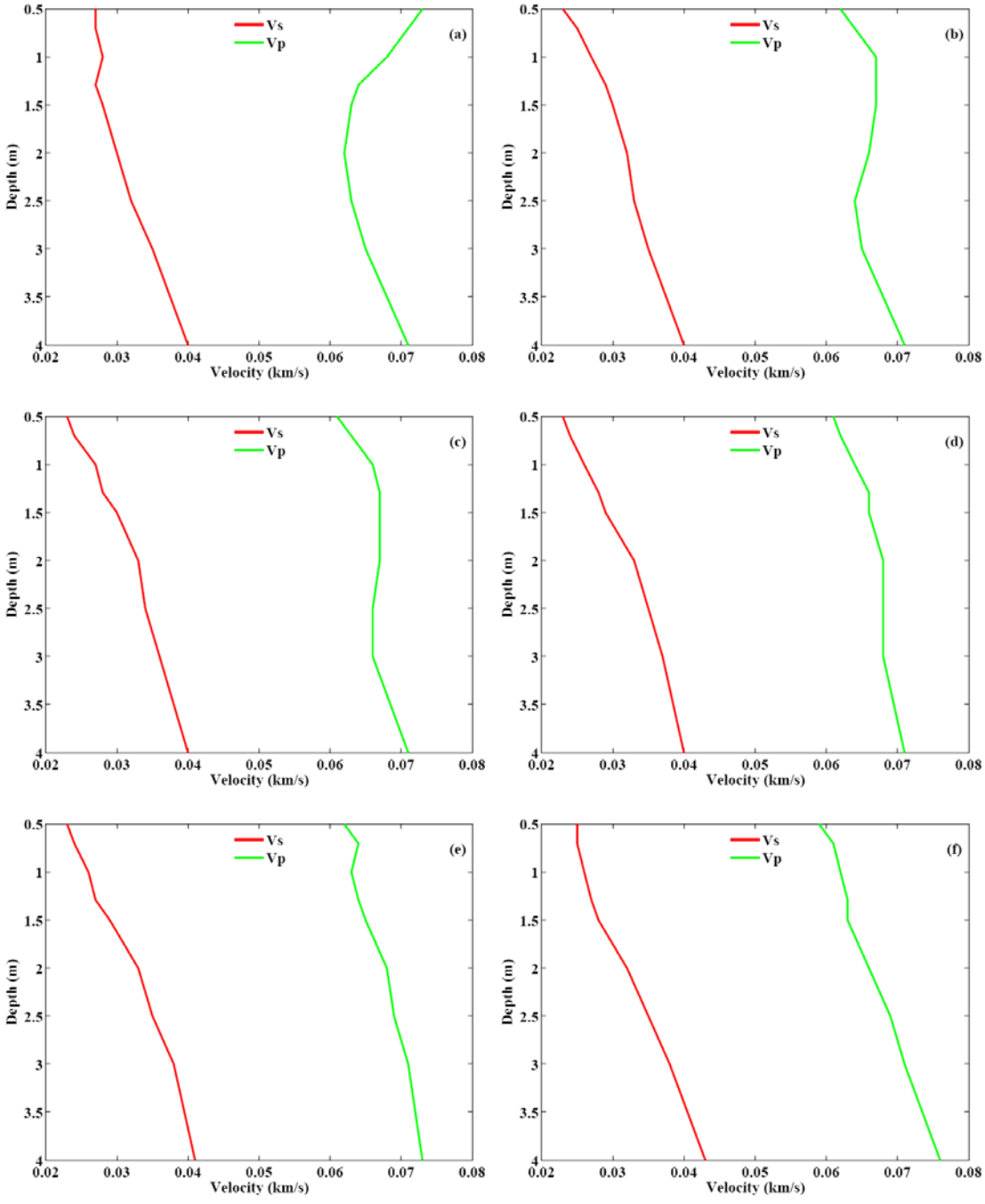

Figure 2.10 *P*- and *S*-wave velocity structures after six sets of perturbations.

2.5.3 Inversion for the Temporal Change

The temporal variations of Rayleigh wave dispersion curves $[\Delta c]$ observed in the experiment are a combination of $[\Delta c_f]$, and their relationship can be derived from:

$$c = c_0 + \Delta c = c_0 + \sum_{i=1}^{N} K_i \Delta c_i \tag{2.6}$$

where c is the phase velocity after injection, c_0 is the original phase velocity before injection, Δc is the change of phase velocity, Δc_i is the perturbation of phase velocity centered at a specific frequency, K_i is the coefficient. The relationship can be expressed in matrix form as:

$$[\Delta c] = [\Delta c_f] \times [K] \tag{2.7}$$

where $[\Delta c]$ is a 10 (frequencies) × 16 (geophones) × 49 (shots) matrix obtained from the field data, and $[\Delta c_f]$ is a 10 (frequencies) × 6 (perturbations) matrix calculated from the modeling. $[K]$ is a 6 (perturbations) × 16 (geophones) × 49 (shots) matrix of coefficients that relate $[\Delta c]$ and $[\Delta c_f]$. Equation 2.7 is used to determine the value of the coefficients matrix $[K]$ by a simple least-square inversion of matrix.

Based on the linear relationship between Rayleigh wave phase velocity and *P*-

and *S*-wave velocities, there is similar relationship between the change of *S*-wave velocity structure during the experiment and the perturbations inserted in the model:

$$V = V_0 + \Delta V = V_0 + \sum_{i=1}^{N} K_i \Delta V_i \tag{2.8}$$

where V is the *S*-wave velocity after injection, V_0 is the original *S*-wave velocity before injection, ΔV is the change of *S*-wave velocity, ΔV_i is the perturbation of *S*-wave velocity centered at a specific depth, K_i is the coefficient. The relationship can be expressed in matrix form as:

$$[\Delta V] = [\Delta V_d] \times [K] \tag{2.9}$$

where $[\Delta V]$ is 41 (depths) × 16 (geophones) × 49 (shots) matrix that needs to be inverted in this study, and $[\Delta V_d]$ is a 41 (depths) × 6 (perturbations) matrix containing 6 sets of Gaussian Function perturbations centered at different depths, and $[K]$ is the same coefficients matrix as in Equation 2.7.

Equation 2.9 is used to obtain the temporal change of *S*-wave velocity structure during the experiment. Here I use a finer depth grid for the perturbations to get higher-resolution *S*-wave velocity structure (from 0 to 4 m underground with an increment of 0.1 m of the area). Figure 2.11 and 2.12 shows the temporal change of *S*-wave velocity for the influenced region under the 9th and 10th geophone where most significant velocity variations occur. A.1 in Appendix is a set of contour plots

showing the changes of 2-D *S*-wave velocity structure of the whole area with the horizontal range from geophone 1 to geophone 16 with a length of 15 m, vertical range from 0 to 4 m underground, and time range from the first shot to the 49th shot with time scale of 49 min. The *S*-wave velocity of the region centered at injection outlet increases up to 4 m/s as the water level increases during injection, and then gradually recovers to the origin value after injection is stopped. There is some irregular noise shown from shot 33 to shot 41 (Time: 33 to 41 min in A.1), which is probably caused by the several incidents that happened during this period as shown in Table 2.1.

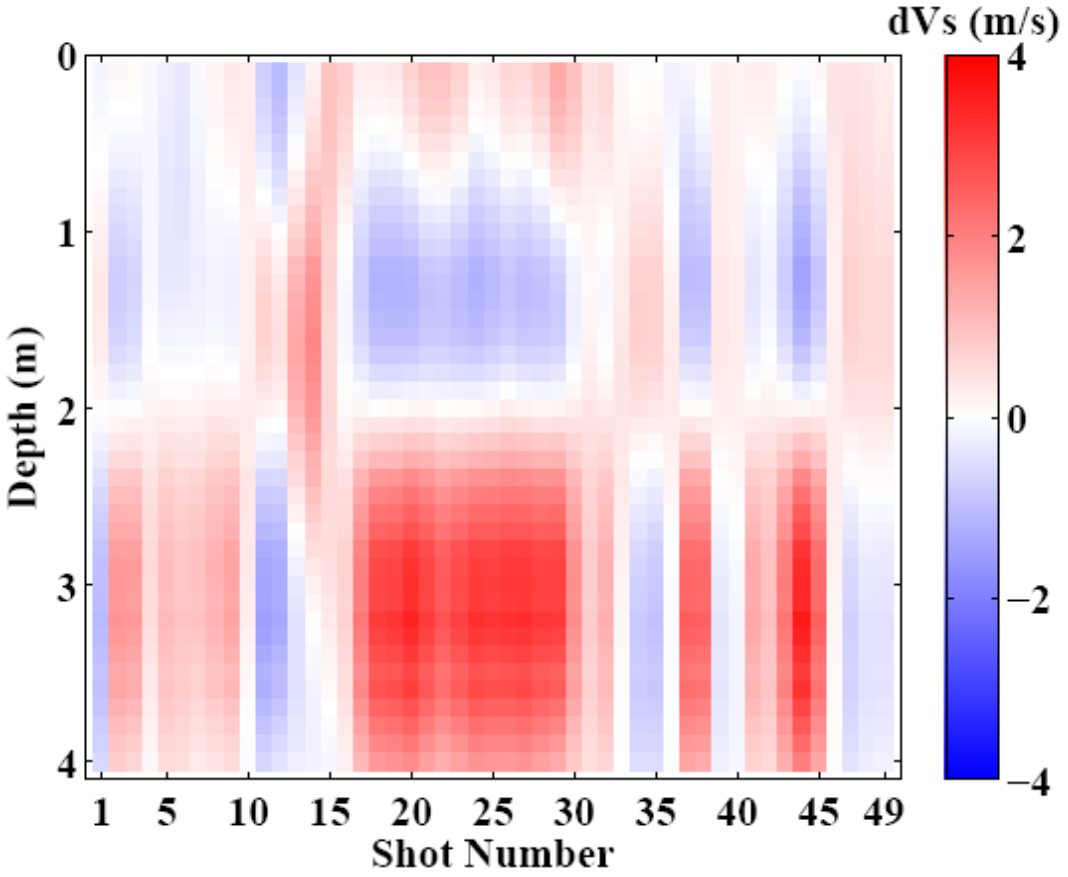

Figure 2.11 Temporal change of *S*-wave velocity for the region under the 9th geophone. Color code is shown in the right.

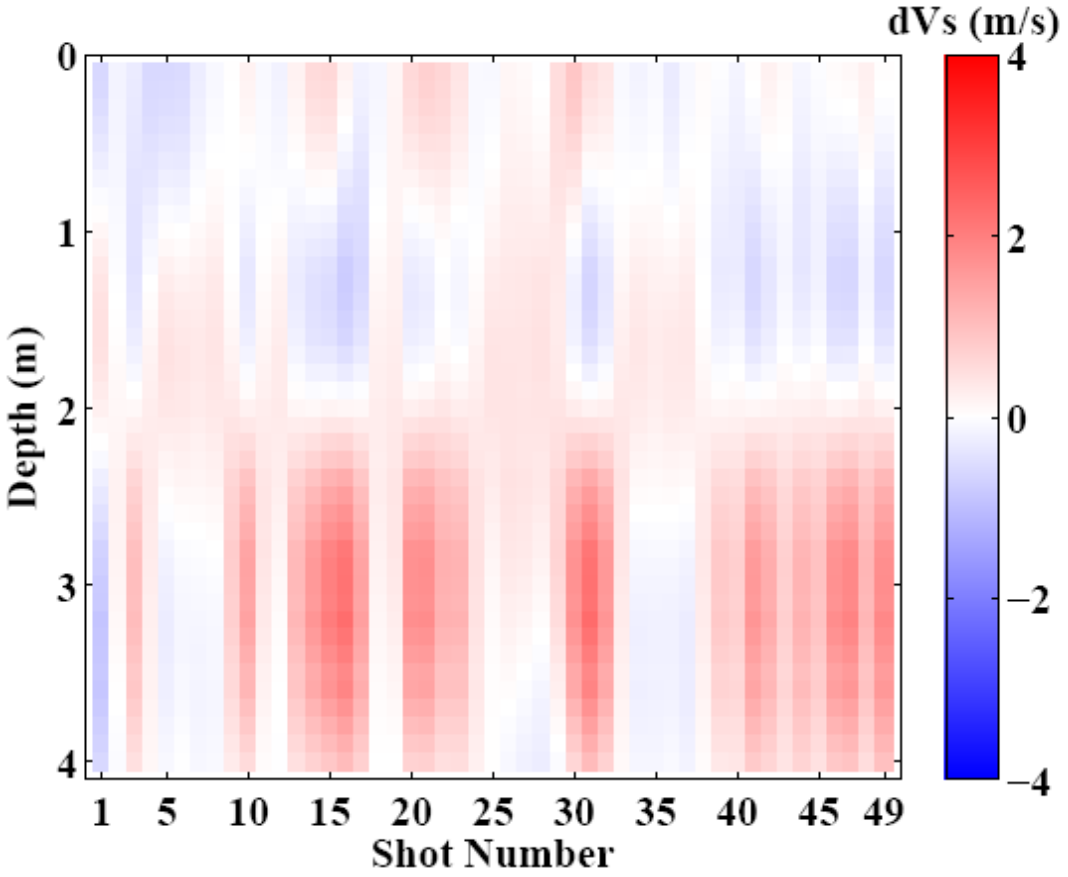

Figure 2.12 Temporal change of *S*-wave velocity for the region under the 10th geophone. Color code is shown in the right.

2.6 Discussions

Little previous field work has been done to measure the relationship between the *S*-wave velocity and the water level in shallow soil layers on the earth's surface. Engineering studies (e.g., Biot, 1956, 1962) generally suggest that the effects of moisture in soils depend largely on whether the material is saturated. The dependence of seismic velocity on water level may vary a lot at different saturation status.

The shallow soil experiment is carried out at Panola Mountain: an exposed

granite outcrop which is covered by a thin soil layer in lower elevations. No evidence of rain or other water source before and during the experiment was observed, which guarantees that our site is not fully saturated. An increase in *S*-wave velocity is observed with rising water level and a decrease of *S*-wave velocity with dropping water level is observed, which is similar to West and Menke (2001)'s result in a partially saturated layer (layer 3 in Figure 2.1). However, this is not consistent with the traditional view that *S*-wave velocity decreases as saturation increases, as observed by Bachrach and Nur (1998). The inconsistency suggests that, in the partially saturated stage, the density of top soil layers may not be significantly changed by the water injection, but the shear modulus should be very sensitive to the change of fluid saturation. The observation in this study can be attributed to an increased fluid-solid interaction upon saturation (Zinszner et al., 1997), which makes it more difficult to apply shear to the medium (i.e., increasing shear modulus).

Abeele et al. (2002) suggest that fluid-induced internal molecular forces may also increase the fraction of active hysteretic units, which enlarge the nonlinear response of the medium. Although in this study, the experiment and the analysis procedure are performed under elastic and linear conditions, this study proposed a practical method to investigate the latent nonlinear effects of the top soil layers and its relationship with fluid saturation.

CHAPTER 3

TEMPORAL CHANGE OF FAULT ZONE SITE RESPONSE ASSOCIATED WITH STRONG GROUND MOTION

3.1 Introduction

In this chapter, I will begin with the definition of fault zone and discuss some fault zone related effects, followed by discussion of a typical method to investigate one common fault zone effect: nonlinear wave propagation. I will briefly describe previous work and then focus on two recent studies. The discrepancy between them gives the motivation of the study described in later chapter.

3.1.1 Fault Zone

A fault is a discontinuity in the earth's surface where two plates pass along each other. The faulting process produces localized belts of fault zone rocks that are fragmented and weaker than the surrounding area. The thickness of a major plate boundary fault zone is around tens to hundreds of meters at the surface but becoming narrower at depths (e.g., Ben-Zion and Sammis, 2003).

Highly damaged fault zone rocks are expected to generate several fault zone related seismic signals, such as fault zone head and trapped waves, anisotropy, scattering and nonlinear wave propagation effects. These signals, in turn, can be used

to quantify spatial-temporal evolutions of fault zone properties at seismological depth.

3.1.2 Previous Work and Motivation

This study focuses on nonlinear wave propagation effects inside active fault zones. Although experimental studies from geotechnical engineers (e.g., Seed and Idriss, 1970; Hardin and Drnevich, 1972a, b) have revealed clear nonlinear elastic properties of shallow stiff-soil sites during strong ground motion for a long time, solid evidence of nonlinearity in the vicinity of fault zones during an earthquake does not emerge until recently. Evidence first comes from quantitative time-dependent measurements of seismic velocities at near fault stations. Poupinet et al. (1984) measured temporal variations of *S*-wave velocity using data from microearthquakes networks near Calaveras Fault, California. An *S*-wave velocity decrease of 0.2% is observed at the south end of the aftershock zone, and they suggested two physical explanations: a tectonic change and a change in the water table.

Dodge and Beroza (1997) analyzed coda waves recorded at 78 stations after the 1989 Mw6.9 Loma Prieta earthquake in California and found that decreases of coseismic velocity mostly occurred in the shallow crust near the stations. They proposed that the velocity decrease is likely caused by crack opening or crack coalescence in the shallow crust due to the strong shaking from the mainshock.

Vidale and Li (2003) monitored the healing process of damage zone on the

shallow Johnson Valley fault after the 1992 Mw7.3 Landers earthquake by observing the recovery of reduced seismic wave velocities in and outside the fault zone. Their results showed that seismic velocity inside the fault zone decreased after the Landers earthquake and then gradually recovered logarithmically in the following several years, while the influence on velocity outside the fault zone is much smaller. They also found that this recovery process is reversed by the 1999 Mw7.1 Hector Mine earthquake, which occurred 20-30 km away. Li et al. (2003) probed the rupture zone of the Hector Mine earthquake using repeated near-surface explosions and found *P*- and *S*-wave travel time delays and gradual recovery after the mainshock. The velocity increase during the healing process appeared to vary for several fault segments with different geological settings. They discussed some possible mechanisms for the healing and suggested that the closure of partially saturated cracks opened during the 1999 earthquake is the most likely mechanism, although the effects of static stress change can not be conclusively ruled out.

Rubinstein and Beroza (2004) used a moving-window waveform cross-correlation to analyze 55 repeating microearthquake sequences on the San Andreas Fault after the Loma Prieta earthquake and find systematic delays up to 20 ms in the direct *S*-wave and 50 ms in the early *S*-wave coda, which are interpreted as reductions in near-surface velocity. They concluded that the strong shaking of the earthquake opens new cracks and enlarges pre-existing cracks in the rock, which in turn reduce seismic velocity. They suggested that the strong ground motion is nonlinear because considerable seismic energy is dissipated in this cracking and

crack-expanding process.

Nishimura et al. (2005) analyzed seismic data from successive explosion experiments at Iwate volcano, Japan after several significant volcanic activities and an Mw6.1 earthquake happened in 1998. They found a reduction of 1% in velocities at frequency range of 3-9 Hz at the time of the earthquake, and there is a gradual recovery with time scale of several years after that.

Rubinstein et al. (2007) analyzed four repeating earthquake sequences after the 2003 Mw8.0 Tokachi-Oki earthquake to identify the velocity changes caused by the mainshock. By using various source-receiver geometries, they found that the most likely places to cause the time delays are near surface regions. Some path effects are also found, but are less significant. After relating the velocity reductions to the strong shaking and site characteristics, they suggested that the reductions are caused by damage to near-surface materials created by strong ground motion.

Beresnev and Wen (1996) give a detailed description of evidences of nonlinear soil response from the seismological studies. Also, in recent years, the spectral ratio method is also applied to investigate the fault zone related nonlinear effects. The spectral ratio of the seismic waves recorded by spatially separated stations or borehole seismometers are used to estimate the site response between the stations or seismometers. Huang et al. (2005) applied the spectral ratio analysis to seismic data recorded by the Dahan downhole array during and after the 1999 Mw7.3 Chi-Chi earthquake and found that the predominant frequency of the Chi-Chi mainshock shifts lower. They also found discrepancies between the synthetic

waveform with linear site response and the observation, which may indicate that nonlinear site effects are induced by the large ground shaking.

Sawazaki et al. (2006) find a reduction of 30% to 70% of the peak frequency by computing the coda spectral ratios using data recorded by vertical borehole arrays during the 2000 Western Tottori and 2003 Tokachi-Oki Earthquake sequences in Japan. They also compared the results from solid rock, weathered rock, and sandy gravel sites and found that the time scale of recovery in the sandy gravel site is much shorter than the other two. In both the solid and weathered rock sites, they observed long-time recovery with time scale of several years.

Karabulut and Bouchon (2007) analyzed ground accelerations recorded at a small array on the Karadere segment of the North Anatolian fault during the 1999 Mw7.1 Düzce earthquake and its early aftershocks. They found strong spatial variability of the ground acceleration inside and outside the fault, and temporal variation of the spectral ratio in three periods after the mainshock. They also compared the observed shifts of peak frequencies with the modeled velocity drops and discussed several mechanisms. They concluded that the linear elastic fault zone properties are soon recovered after the strong shaking is diminished. The proposed mechanism for their conclusion is no creation of new cracks but just changes in the configurations of the pre-existing cracks.

Karabulut and Bouchon (2007) found instant recovery in fault zone while Sawazaki et al. (2006) found much larger delay at several sites. This difference indicates that the nonlinear site response in fault zone site response still needs further

investigation. In this chapter, I examine temporal changes in fault zone site response in the same region as Karabulut and Bouchon (2007), but there are two major differences: (1) A much longer recording from eight days before to three months after the Düzce mainshock is used. So this study has a better resolution on the postseismic recovery than Karabulut and Bouchon (2007). (2) I found a much larger recovery with a time scale of several months, as compared to instant recovery found by Karabulut and Bouchon (2007).

In the following sections, I will first describe the tectonic environment and then the analysis procedure. Finally I will discuss some possible mechanisms and compare the results with those from previous studies.

3.2 Tectonics Environment

The NAF in Turkey is one of the active fault zones in the world. As the Arabian and the Eurasian plates move together, the Anatolian micro plate is extended westward along the NAF at a rate about 20 mm per year (Relinger et al., 1997). The Mw7.4 İzmit earthquake struck northwestern Turkey on August 17, 1999. Three months later, the Mw7.1 Düzce earthquake occurred 100 km to the east of the epicenter of the İzmit earthquake (Figure 3.1). These adjacent major earthquakes are followed by numerous aftershocks, and hence provide good seismic data to investigate the temporal change of fault zone site response.

The analysis employs strong motion seismic data recorded by two stations VO

and FP from a temporary 10-station PASSCAL seismic network along and around the Karadere-Düzce branch of NAF (Seeber et al., 2000; Ben-Zion et al., 2003). Both stations have REFTEK recorders, three-component L22 short-period sensors with a sampling frequency of 100 Hz, and three-component force-balance accelerometers. Station VO is located inside the rupture zone, while station FP is about 300 m away (Figure 3.1). The fault zone has a width of about 100 m, and the average shear wave velocities inside and outside the fault zone are around 1500 m/s and 3200 m/s, respectively (Ben-Zion et al. 2003). Strong ground motions caused by the Düzce Earthquake (Mw7.1, November 12, 1999) is recorded by both VO and FP stations.

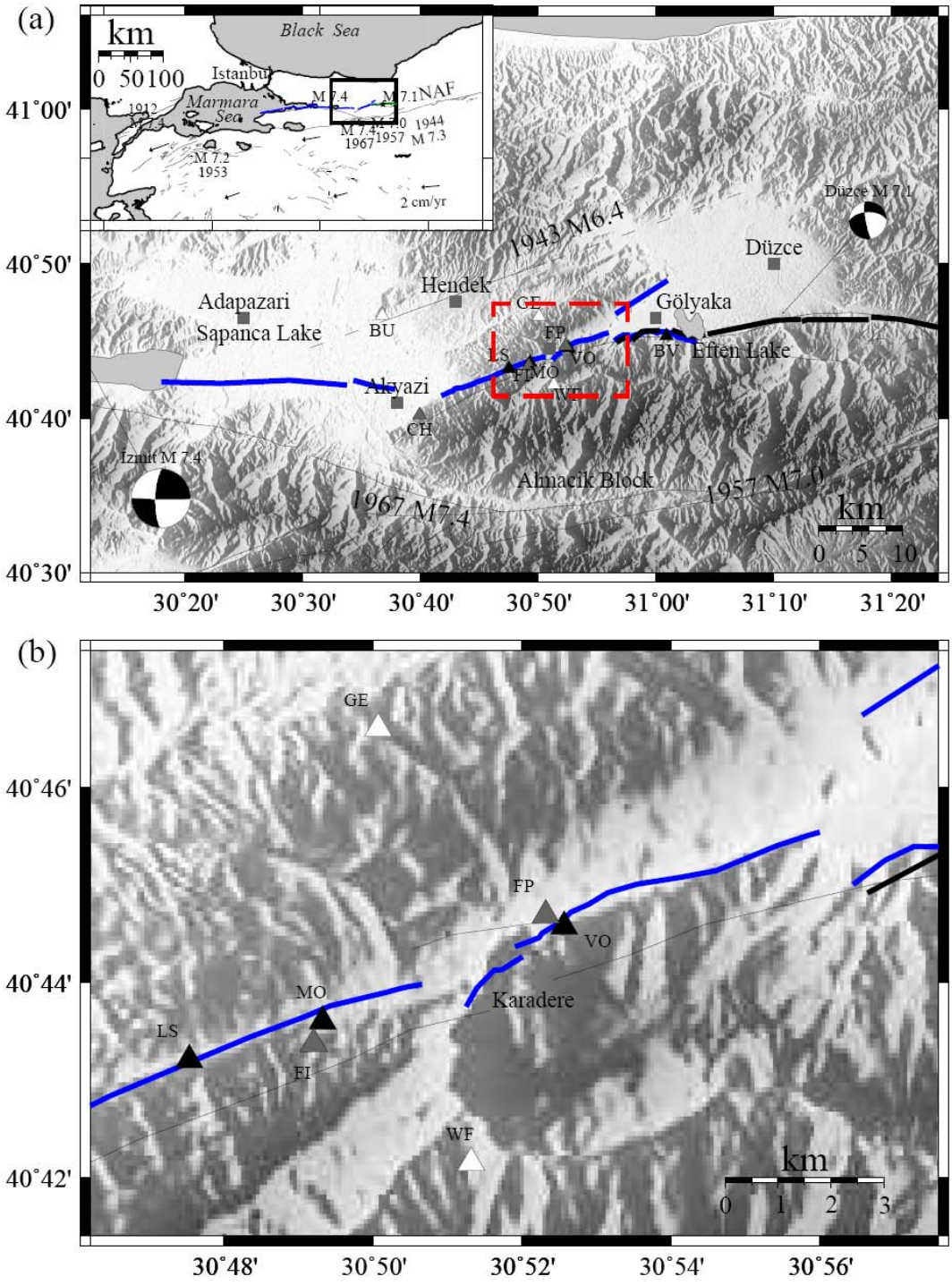

Figure 3.1 (a) Topography map of the area along the Karadere-Düzce branch of the NAF. Shaded background indicates topography with white being low and dark being high. The surface ruptures of the Ízmit and Düzce earthquakes are indicated with blue and black lines, respectively. Dark thin lines associated with earthquake information denote faults that were active during recent ruptures. Other dark thin lines are geologically inferred fault traces. Stations within, near, and outside the fault zone are shaded with dark, gray, and white triangles, respectively. Gray squares denote

locations of nearby cities. The area bounded by the red dashed lines is shown in (b). The inset illustrates the tectonic environment in northwestern Turkey with the box corresponding to our study area. Vectors represent plate deformation rate (Reilinger et al., 1997) from GPS data. Modified from Peng and Ben-Zion (2006). (b) Zoom-in map of the fault area along Karadere fault and the location of the station VO inside the fault and FP about 300 m away from the fault. All the symbols and notations are the same as in (a).

3.3 Analysis Procedure

Two horizontal component ground acceleration records at stations VO and FP generated by 1806 earthquakes are used in this study. These include 113 events before the Düzce mainshock, the mainshock, and 1692 events after the mainshock. The occurrence time of these earthquakes ranges from 8 days before to 3 months after the Düzce mainshock. The local magnitudes of most aftershocks range from 0 to 5, and the depths of the sources range from 5 to 15 km. The first 91 events are not used due to bad recordings at station FP in this period (before November 4, 1999).

The following two dataset are analyzed in this study: the whole dataset which includes all possible waveform parts, and those only recorded during the coda wave window of earthquakes. To utilize the whole dataset, I design a 10-second time window and slide it through seismic records at station VO and FP and slide 5 seconds each step. The coda wave window is defined as starting from twice the direct *S*-wave travel time after the origin time of each event, with length of 10 seconds. To avoid mixing waves of different events, if there is any other event between the onset of the *S*-wave and the end of the coda window of one event, or the phases cannot be clearly

identified, the records of this event are not used.

Next I remove the mean value of the traces, and apply a symmetric 5% cosine taper. After using FFT to transform the traces into frequency domain, I sum up the power spectra of the two horizontal components (North-South and East-West) and then take the square root to get the amplitude of vector sum of the two horizontal spectra (average horizontal spectra). The obtained spectra are smoothed using a box car with a half width of five points. The spectral ratio is obtained by taking the ratio of the average horizontal spectra from station VO and FP. An example is shown in Figure 3.2 to illustrate the analysis procedure.

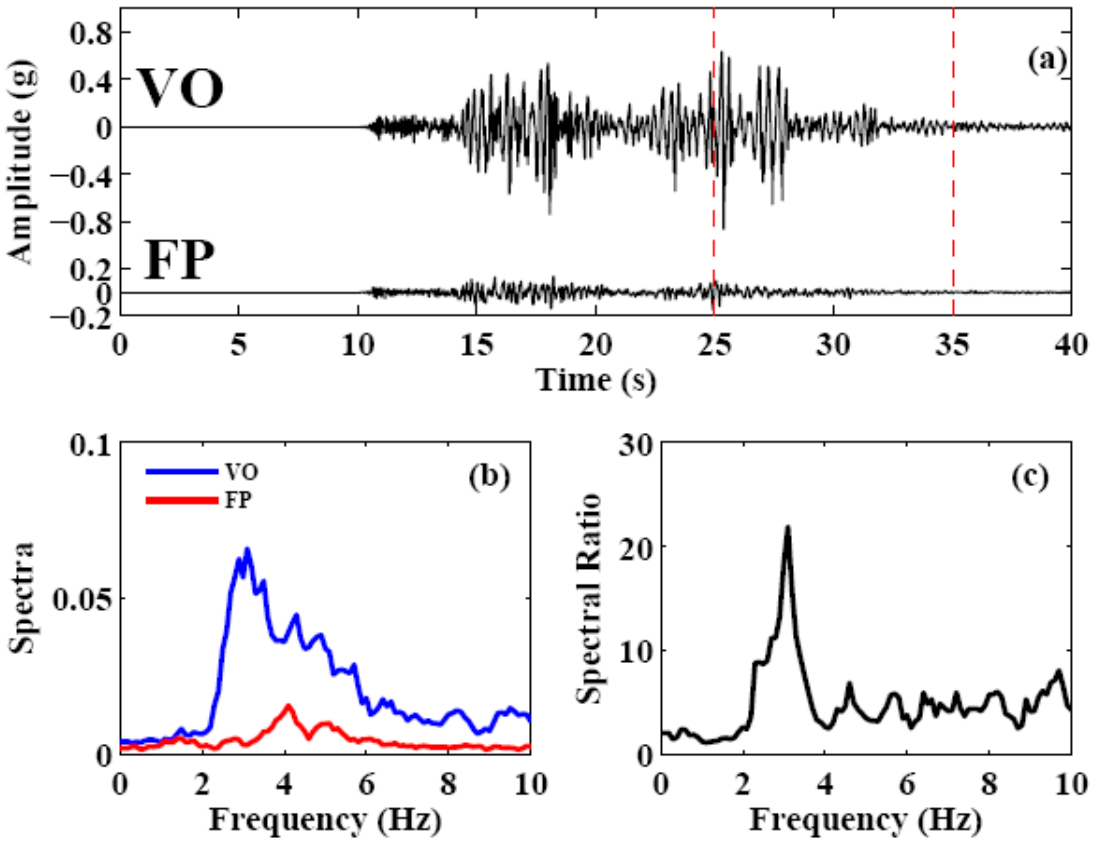

Figure 3.2 (a) Ground accelerations recorded during the main shock of 1999 Mw7.1 Düzce, Turkey, earthquake recorded at the two stations VO and FP. The red dashed lines indicate the selected 10s window. (b) Acceleration spectra and (c) spectral ratio during the main shock at the two stations VO and FP.

3.4 Results

After processing all the data, I obtain spectral ratios for 7543 matched 10s windows, including 390 windows for the events before the Düzce mainshock, 7 for the mainshock, and 7147 for events after the mainshock. By analyzing the coda part, I obtain spectral ratios for 697 matched 10s windows, including 54 windows for the events before the main shock and 643 for events after the main shock. Figure 3.3 shows a comparison of spectral ratios for the direct *S*-wave and the coda waves for 15

events 2 hours after the mainshock. The temporal change of spectral ratio for all and coda wave only are shown in Figure 3.4 and 3.5, respectively. A clear spectral ratio increase and peak frequency drop is shown at the time of mainshock, followed by gradual recovery in both data sets.

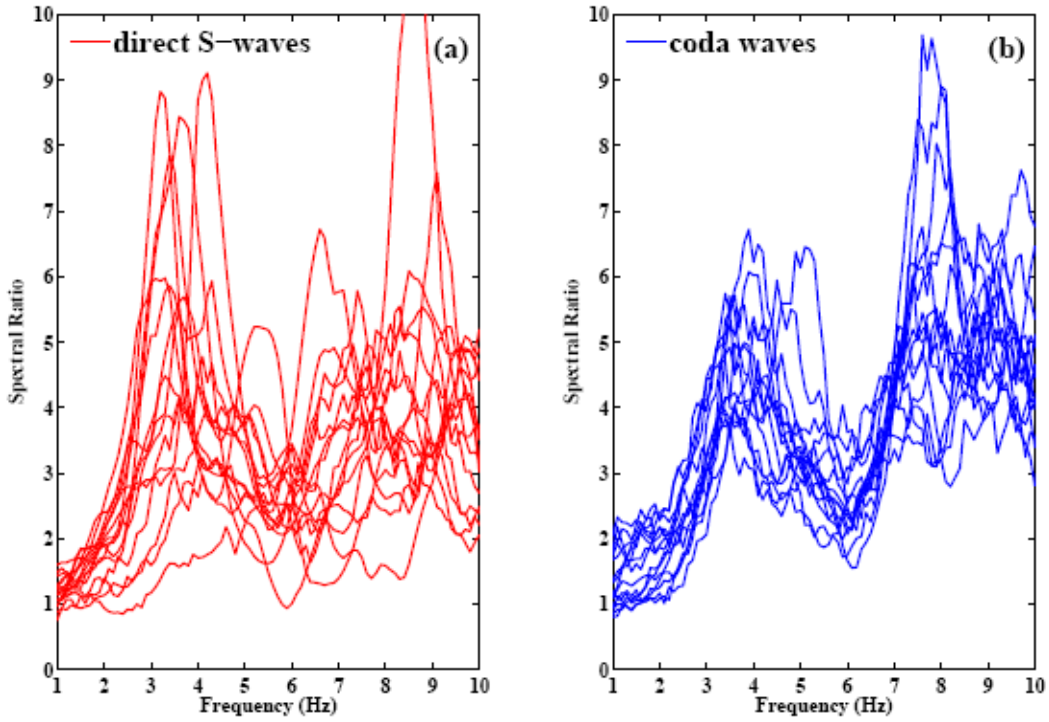

Figure 3.3 Spectral ratio traces of (a) direct S-waves and (b) coda waves of 15 events which occurred two hours after the mainshock of 1999 Mw7.1 Düzce, Turkey, earthquake, recorded at station VO and FP.

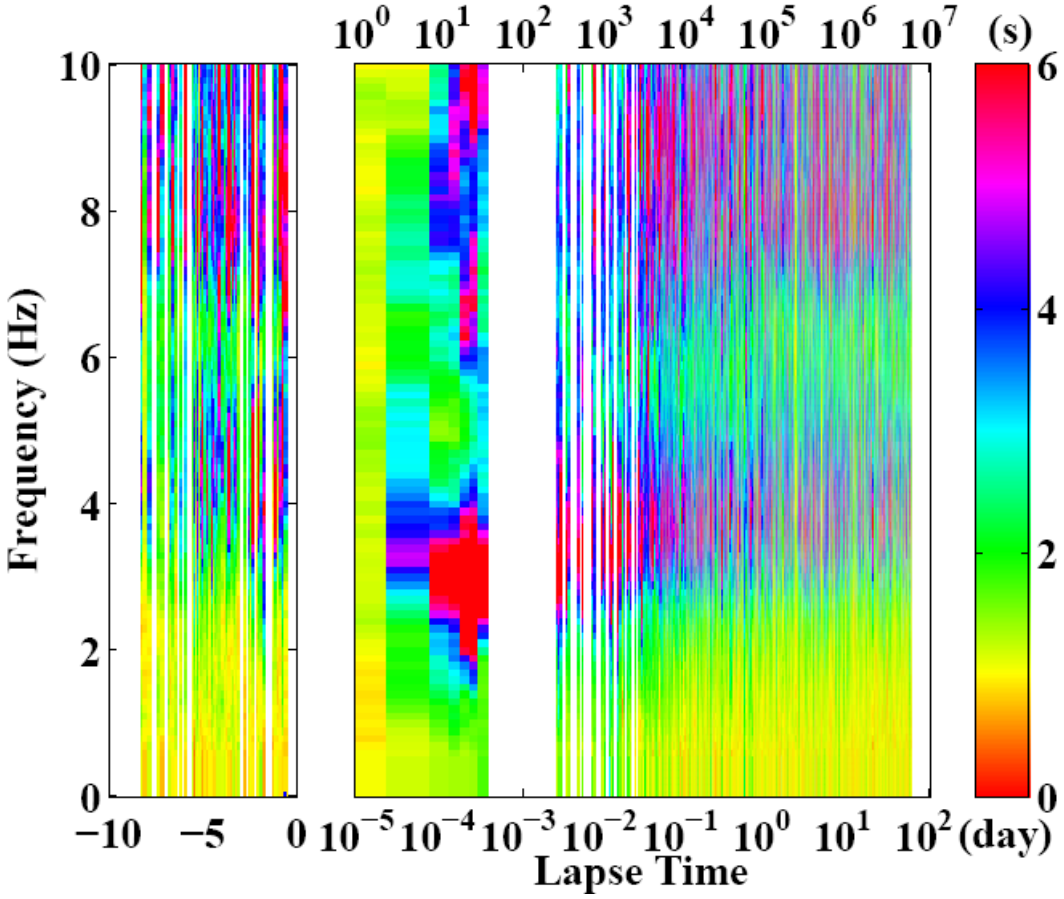

Figure 3.4 Temporal changes of spectral ratio at station VO and FP for the 1999 Mw7.1 Düzce, Turkey, earthquake. The right bin shows the running spectral ratio by color code for the main shock and aftershocks. The left bin shows that for the foreshocks. Values shown on the top and bottom of the abscissa indicate lapse times after the main shock in seconds and in days, respectively. White color represents no data.

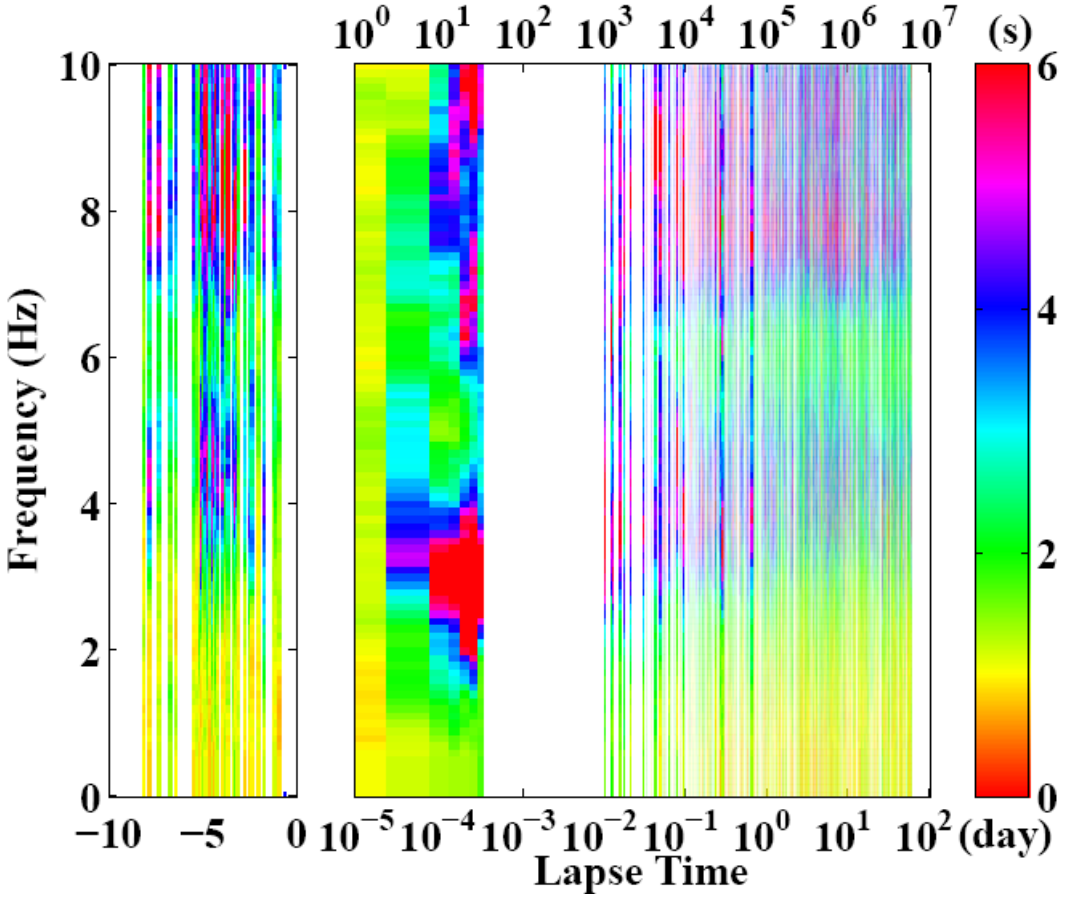

Figure 3.5 Temporal changes of coda spectral ratio at station VO and FP for the 1999 Mw7.1 Düzce, Turkey, earthquake. Symbols and notations are the same as Figure 3.4.

To better quantify the value and time scale of the recovery process, I divide the time range after the main shock into six periods: 0-30 s, 100-1000 s, 0.3-2 hours, 0.1-1 days, 1-10 days, and 10-80 days after the main shock, which are near equally distributed in the logarithmic time domain. Logarithmic time is used instead of linear time because previous studies have found logarithmical healing process for long-term recovery of nonlinear effects (e.g., Peng and Ben-Zion, 2006; Sawazaki et al., 2006). Next I stack all the spectral ratio traces in each period. I also stack all the traces before the mainshock. Using these averaged spectral ratio traces, I identify the values

of the highest spectral ratios and peak frequencies. I also apply this procedure to all the coda spectral ratio traces. Unfortunately, there are gaps at 0-30s and 100-1000s after the main shock because no trace exists in those periods.

The averaged spectral ratio traces are shown in Figure 3.6. For comparison, the averaged traces immediately after the main shock from all the data are included in the coda results for. Table 3.1 lists the peak spectral ratios, peak frequencies, and the reduction or recovery rate for each period. The averaged spectral ratios from coda waves generally show lower overall values, but with a higher value of peak frequency.

The results show a shift of the spectral peak to lower frequencies during the main shock. The peak frequency reduces from 4.3 Hz several days before the main shock to 2.9 Hz (67.4% of the pre mainshock value) right after the mainshock. It quickly recovers to 3.8 Hz (64% recovery of the dropped value) after a day, and then gradually recovers to 4.0 Hz (79% recovery of the dropped value) after 72 days.

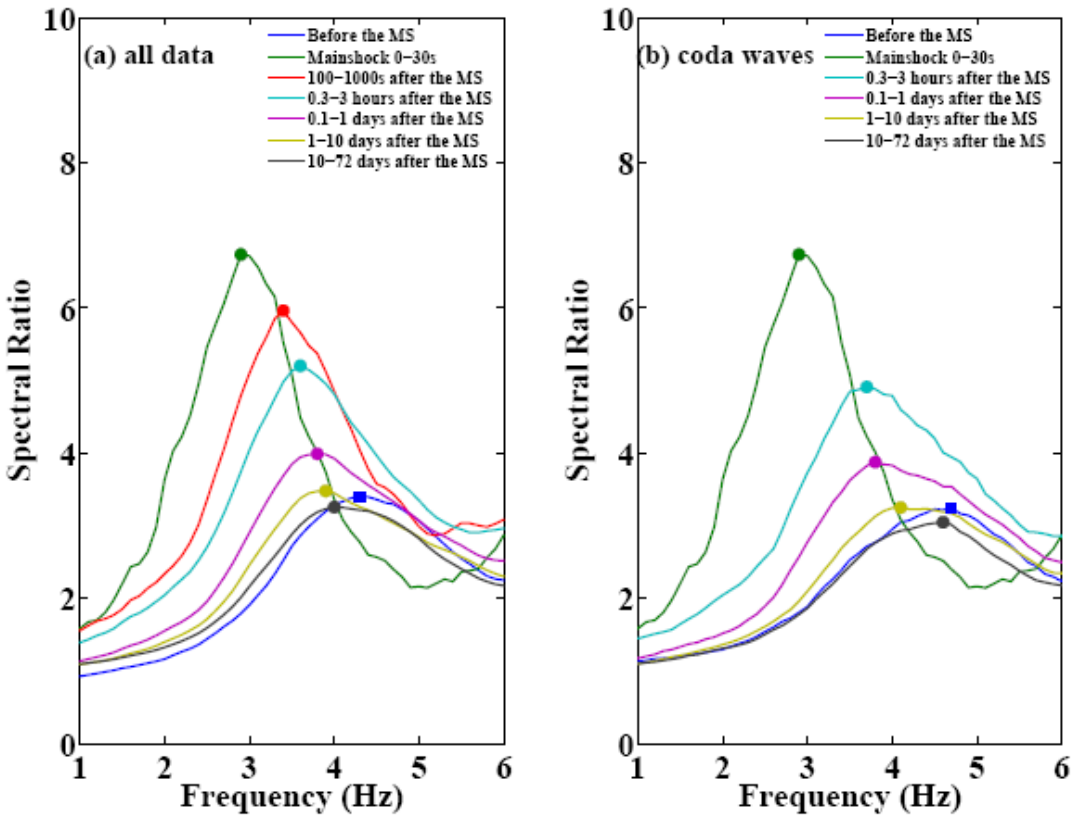

Figure 3.6 (a) Logarithmically averaged spectral ratios for the foreshocks (blue), main shock (green), and the aftershocks on different periods: 100-1000s (red), 0.3-2 hours (cyan), 0.1-1 days (magenta), 1-10 days (yellow), and 10-80 days (black) of 1999 Mw7.1 Düzce, Turkey, earthquake, recorded at station VO and FP. (b) Logarithmically averaged coda spectral ratios with the same color code. The peaks of averaged spectral ratios for the events before the mainshock are shown in filled blue squares, and those for mainshock and events after that are shown in filled circles with other colors.

Table 3.1 The peak spectral ratios, peak frequencies, and the reduction or recovery rate for each period, (a) for all the data and (b) for the coda part.

(a) ALL the Data			
Time Period	Peak Spectral Ratio	Peak Frequency (Hz)	Reduction/Recovery Rate
Before the mainshock	3.4	4.3	
Mainshock 0-30s	6.7	2.9	30% reduction
100-1000s after the mainshock	6	3.4	35% recovery
0.3-3 hours after the mainshock	5.2	3.6	50% recovery
0.1-1 days after the mainshock	4	3.8	64% recovery
1-10 days after the mainshock	3.5	3.9	71% recovery
10-80 days after the mainshock	3.3	4	79% recovery
(b) Coda Part			
Time Period	Peak Spectral Ratio	Peak Frequency (Hz)	Reduction/Recovery Rate
Before the main shock	3.3	4.7	
Mainshock 0-30s	6.7	2.9	38% reduction
0.3-3 hours after the mainshock	4.9	3.7	44% recovery
0.1-1 days after the mainshock	3.8	3.8	50% recovery
1-10 days after the mainshock	3.3	4.1	67% recovery
10-80 days after the mainshock	3	4.6	94% recovery

3.5 Discussion

3.5.1 Comparison of Direct *S*-wave and Coda Waves

The spectral ratio calculated from direct *S*-waves and coda waves are compared in Figure 3.3. The comparison indicates that spectral ratios calculated from coda waves are generally similar to those calculated from the direct *S*-waves, but with less scatter. This is consistent with the observations by Sawazaki et al. (2006) and Mayeda et al. (2007). This phenomenon can be attributed to the randomly distributed incident angles and back azimuths of wavelets constituting coda waves by assuming that it consists of waves that have been backscattered from random heterogeneities distributed throughout the medium (Aki, 1969). Such random distribution provides an averaging effect for the observed spectral ratios by making them less dependent on propagation paths than the direct *S*-wave.

The disadvantage of using only the coda part is that data in certain time range (e.g., immediately after the main shock) may be lost for the reason that there are so many events thus the coda parts are mixed with other events and not easily extracted. For this reason the results from both measurements are kept for comparison.

Coda waves are basically from the scattered energy in the media. In the highly fractured fault zone, it is much easier for the waves with shorter wavelengths to be scattered and then be received as the coda part of the arrivals (Aki and Chouet, 1975). Then assuming a constant wave velocity which is only determined by media property,

it is known that the coda waves with shorter wavelengths should also have higher frequencies. Waves with higher frequencies would attenuate faster than those with lower frequencies, and this can explain why we observed lower value of spectral ratio for coda waves, which suggests a de-amplification effect.

3.5.2 Possible Mechanisms

Many experimental and modeling studies have been done to investigate the nonlinearity of soil response (Jarpe et al., 1988, 1989; Seed, 1988; Chang et al., 1990; Mayeda et al., 1991; Yu et al., 1992). The prevailing observation is that large stains decrease the seismic wave velocity and increase the damping. In frequency domain, this corresponds to shift of frequency to lower values and reduction in peak value. The peak frequency drop we observed is consistent with the previous observations. However, we observe a sudden increase of the spectral ratio of VO to FP at the time of the Düzce mainshock, which is not consistent with the results in soil response, but is similar to the result of Karabulut and Bouchon (2007) in the same region. Results from both studies indicate that the physical mechanism assumed in the conventional laboratory studies cannot work well for the highly fractured fault zone. In this section, I will discuss other possible mechanisms that would explain our results.

Many factors can change the amplification of ground motion in the fault zone: geometric and elastic properties of the fault zone, directivity of sources, shallow layer structures, radiation and path effects. Because the two stations are very close to each

other (about 300 m) compared to the distances between earthquakes sources and stations (more than 10 km), every source could be considered as the same for the two stations. So the source and propagation effects are unlikely to be the reason for the observed temporal changes. The presence of hard rock outcrops near the two stations (Karabulut and Bouchon, 2007) can significantly eliminate the shallow sediments effect, which is a usual mechanism of amplification or nonlinearity in previous studies (e.g., Pavlenko and Irikura, 2002).

Temporal change of fault zone properties caused by the nonlinear peak strong ground motion is the most likely cause of the observed changes in spectral ratio and peak frequency. One possible mechanism of nonlinear strong ground motion is cracking or opening of pre-existing cracks inside the fault zone (Dodge and Beroza, 1997; Vidale and Li, 2003; Li et al., 2003; Peng and Ben-Zion, 2004; Rubinstein and Beroza, 2004; Karabulut and Bouchon, 2007) as shown in Figure 3.7. During strong ground motions, the opening of cracks can significantly reduce the elastic modulus of the medium and therefore decrease the seismic velocities inside the fault zone. This would increase the contrast of the seismic velocity inside and outside the fault zone, and hence enlarge the amplification due to the conservation of seismic energy, although part of the seismic energy is consumed in the cracking and crack-expanding processes.

The gradual recovery (with a scale of several months) we observed is characteristic of solid rock site. No such long time recovery has been found at sandy gravel sites or other relatively softer sites before (e.g., Sawazaki et al., 2006). This is

also supported by the geological survey results showing that the region around the Karadere-Düzce branch of the NAF is hilly with mostly hard rock outcrops but little sedimentary cover (Karabulut and Bouchon, 2007).

Underground fluid flow is another important factor that could change the fault zone elastic properties (Vidale and Li, 2003; Li et al., 2003). Abeele et al. (2002) provide evidence from several experiments indicating that nonlinear response is significantly increased by water saturation, especially in rocks containing small pore systems. The existence of a large amount of underground water may cause more significant change of site response with up to 70% reduction of peak frequency than drier sites with around 30% reduction of peak frequency (Sawazaki et al., 2006).

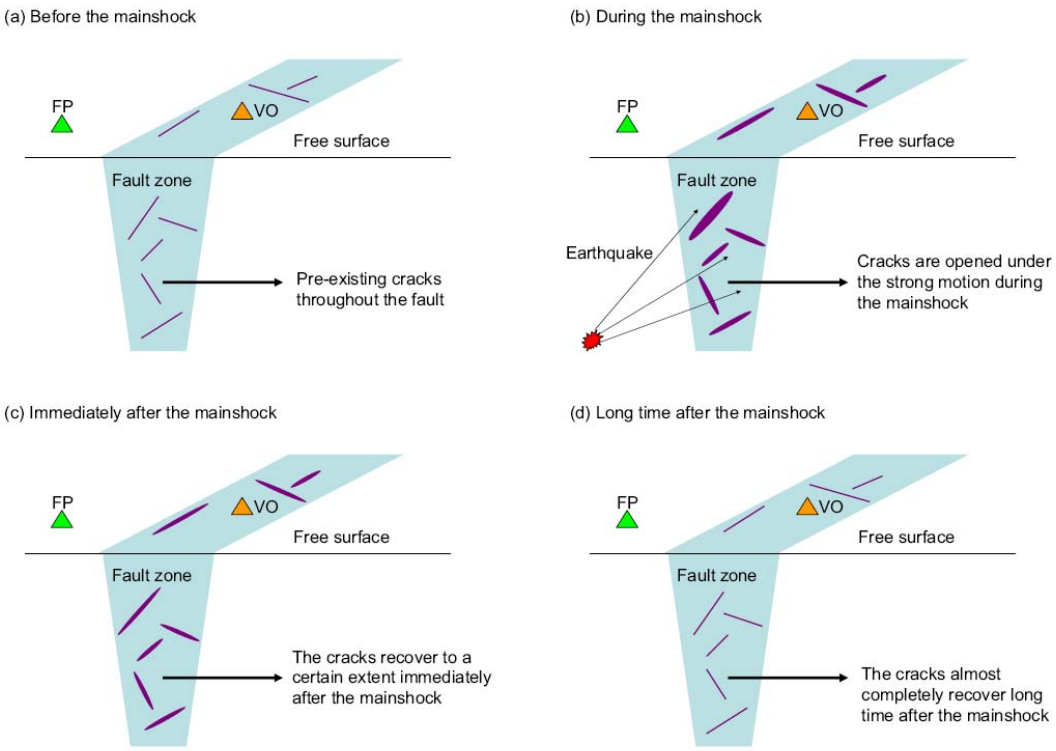

Figure 3.7 Schematic illustration of one possible physical mechanism for nonlinearity in the fault zone: cracking or opening of pre-existing cracks throughout the fault zone.

3.5.3 Comparison with Previous Studies

Assuming a low velocity fault zone sandwiched between two half-spaces, the relationship between resonant frequency f and wave velocity V is given by Equation 3.1:

$$f = \frac{V}{2H} \tag{3.1}$$

where H is the thickness of the fault zone. If we assume that H does not change

over time, the change of seismic velocity, ΔV is

$$\Delta V = 2H \times \Delta f \tag{3.2}$$

where Δf is the change of resonance frequency.

Many researchers have found delays of seismic wave arrival time in the fault zone using repeated events or artificial explosions after big earthquakes (e.g., Rubinstein and Beroza, 2004; Nishimura et al., 2005; Peng and Ben-Zion, 2006; Rubinstein et al., 2007). Their results generally show sudden increase of arrival time delay for the *S*-wave and *S* wave coda, which suggests seismic velocity reduction. Our result shows peak frequency drop after the main shock, which is consistent with the seismic velocity reduction for their direct ratio relationship.

Peng and Ben-Zion (2006) used a moving window waveform cross-correlation technique to monitor the temporal change of seismic velocity along the Karadere-Düzce branch of the North Anatolian Fault (NAF) using repeated earthquakes after the 1999 İzmit and Düzce earthquakes in Turkey. They found clear step-like delay and logarithmic-type recovery in direct *S* and early *S*-coda waves, which also are attributed to the strong ground motion in the vicinity of the ruptured fault zones. Using Equation 3.2, the percentage velocity drop corresponding to the frequency shift can be estimated. However, the percentage velocity drop we found is with a larger scale than the result of Peng and Ben-Zion (2006). This is most likely due to different time scales. The observation in this study starts immediately after the

mainshock, while Peng and Ben-Zion (2006)'s earliest data is nearly half a day after the mainshock.

Studies concerning the change of site amplification factor with the PGA (Peak Ground Acceleration) (e.g., Chin and Aki, 1991) report change of amplification factor after the PGA exceeds 100-300 gal. In our case the maximum acceleration recorded inside the fault zone during the main shock is around 900 gal which certainly exceeds the criteria of 100-300 gal.

3.6 Conclusion

Applying the spectral ratio method to strong motion accelerations recorded by a pair of stations installed inside and outside the Karadere-Düzce branch of the NAF that ruptured during the 1999 İzmit earthquake, I successfully detected temporal change of site response associated with the strong ground motion of the nearby Düzce earthquake. During the Düzce mainshock, the peak spectral ratio increased from 3.4 to 6.7 and the peak frequency dropped from 4.3 to 2.9. Gradual recovery with time scale of several months is observed after that. The temporal variation of the spectral ratio and peak frequency is associated with the nonlinear ground motion induced by the Düzce earthquake.

Most of the previous spectral ratio studies are limited to vertical borehole arrays and using only coda waves. Results of this study demonstrate that the spectra ratio method can be applied in various aspects of fault zone site response monitoring,

and information can be extracted from the whole seismic recording including direct arrival waves, the coda waves, and even the seismic noises rather than only the coda part, although the spectral ratio of whole data set is not as stable as the coda spectral ratio.

CHAPER 4

SUMMARY

Although many efforts have been made in the last several decades to investigate the nonlinear site effects and many seismological evidences have been provided, the nonlinear site effects are still poorly described and modeled, and the mechanism of the nonlinearity is still not clear. Since the nonlinear systems are much more complicated in nature than linear ones, most previous studies on nonlinear effects are focused on experiments and observations. It is important to study nonlinear response at different scales and locations to fully understand the underlying physical mechanisms.

One practical way of quantifying nonlinear site response is to study temporal changes in material properties. This basic idea originated from the nature of nonlinear effects, which means some initial property of the object has been irreversibly changed due to increasing input amplitude.

In the first study I monitored the temporal change of *S*-wave velocity structure in very shallow soil layers before and after the water level changes. In the second study I measured temporal change of fault zone site response associated with strong ground motion of nearby large earthquakes using the spectral ratio approach. Although the space-time scale, material property, and the employed techniques are different for these two studies, the results may give some common indications on the widely existed nonlinear effects. In the first study, all the procedures are based on a

linear model of seismic velocities. But the mechanism (change in saturation) for the temporal variation of *S*-wave velocity could be caused in part by the nonlinear deformation of rocks or soils. This work suggests that the nonlinear wave propagation effects in top soil layers might be observed if the input amplitude is also changing with time. In the second study, temporal variation of the spectral ratio and peak frequency is related to the nonlinear site effects during the passage of seismic waves caused by nearby major earthquake, so the observation provide further evidence for nonlinear wave propagation effects, which is important for understanding earthquake dynamics and fault healing, as well as localized site effects that may preferentially destroy some structures and regions in large events.

.

APPENDIX

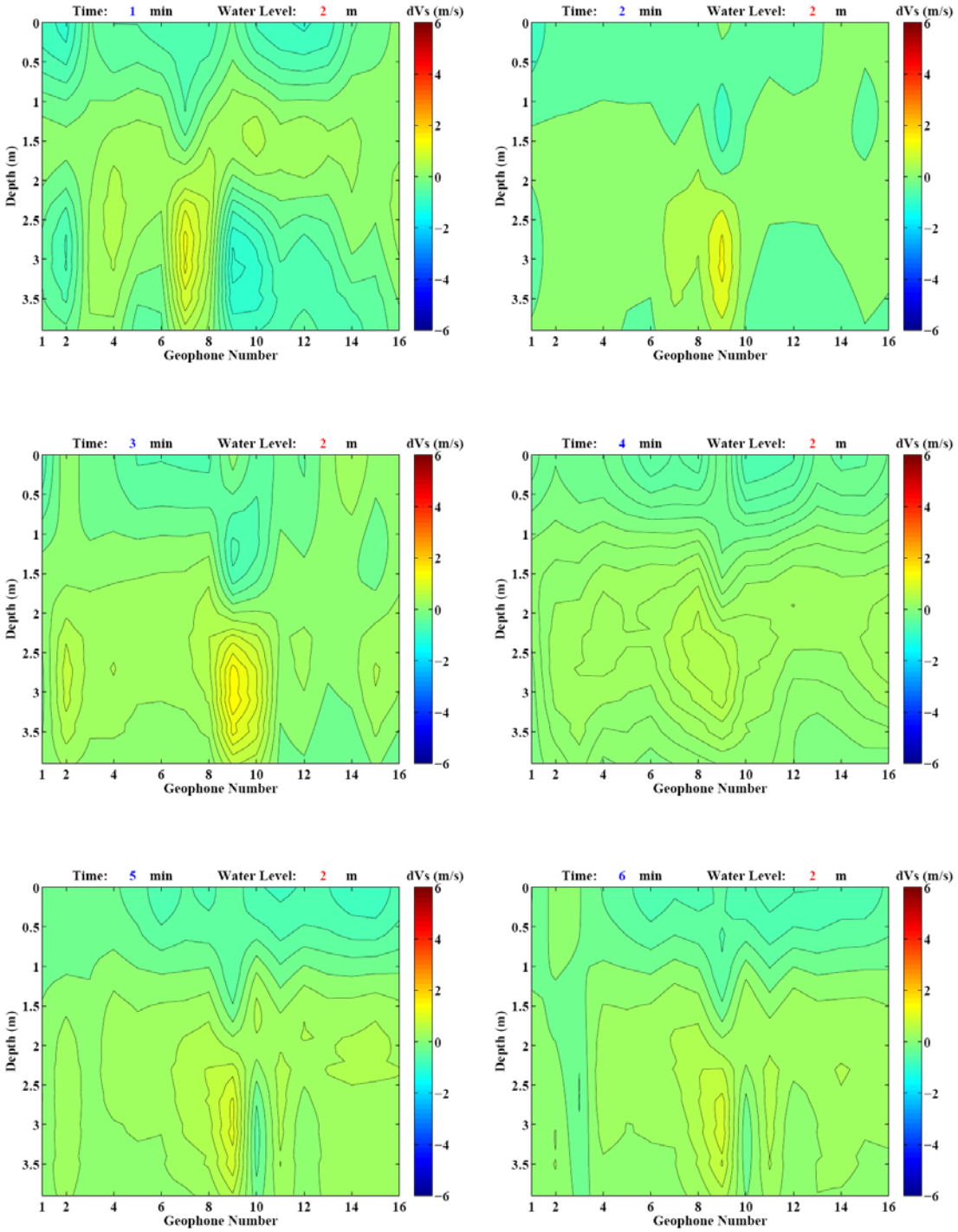

A.1 Contour plots showing the temporal change of 2-D *S*-wave velocity structure. The color bar shows the value of *S*-wave velocity change (positive value means velocity increase, and negative value means velocity decrease), and there is a time indicator at the upper left and a water level indicator at the upper right of the figure.

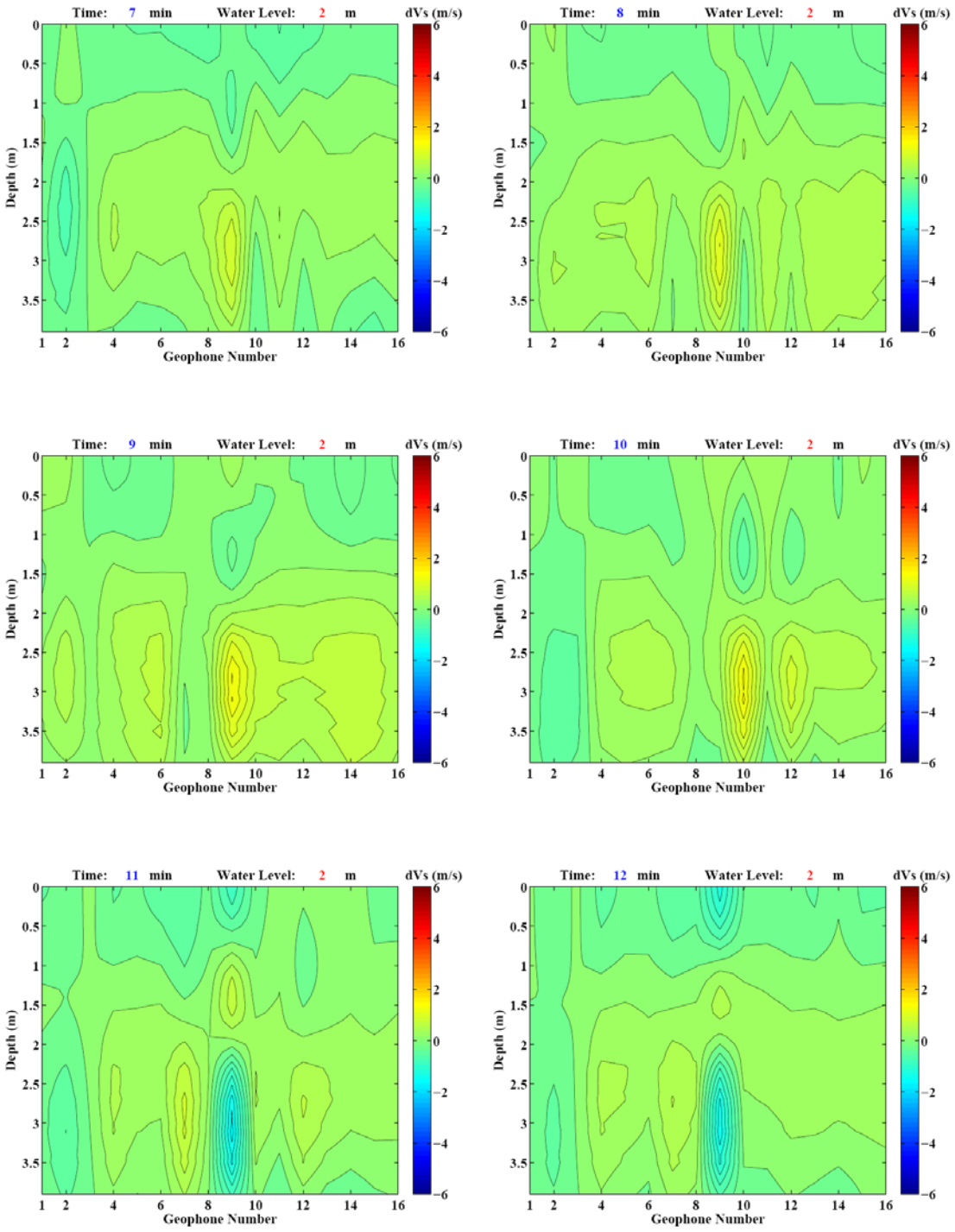

A.1 (continued).

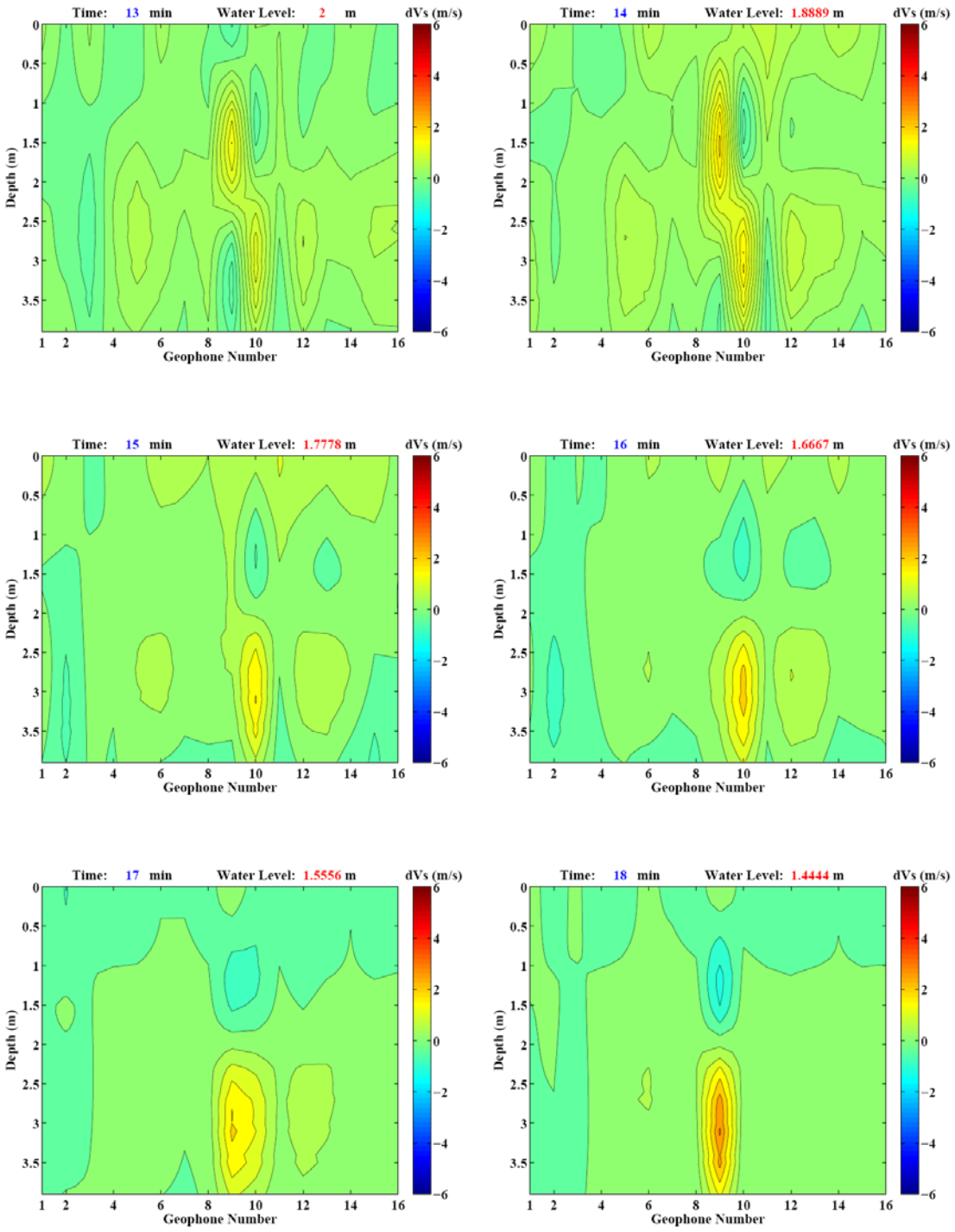

A.1 (continued).

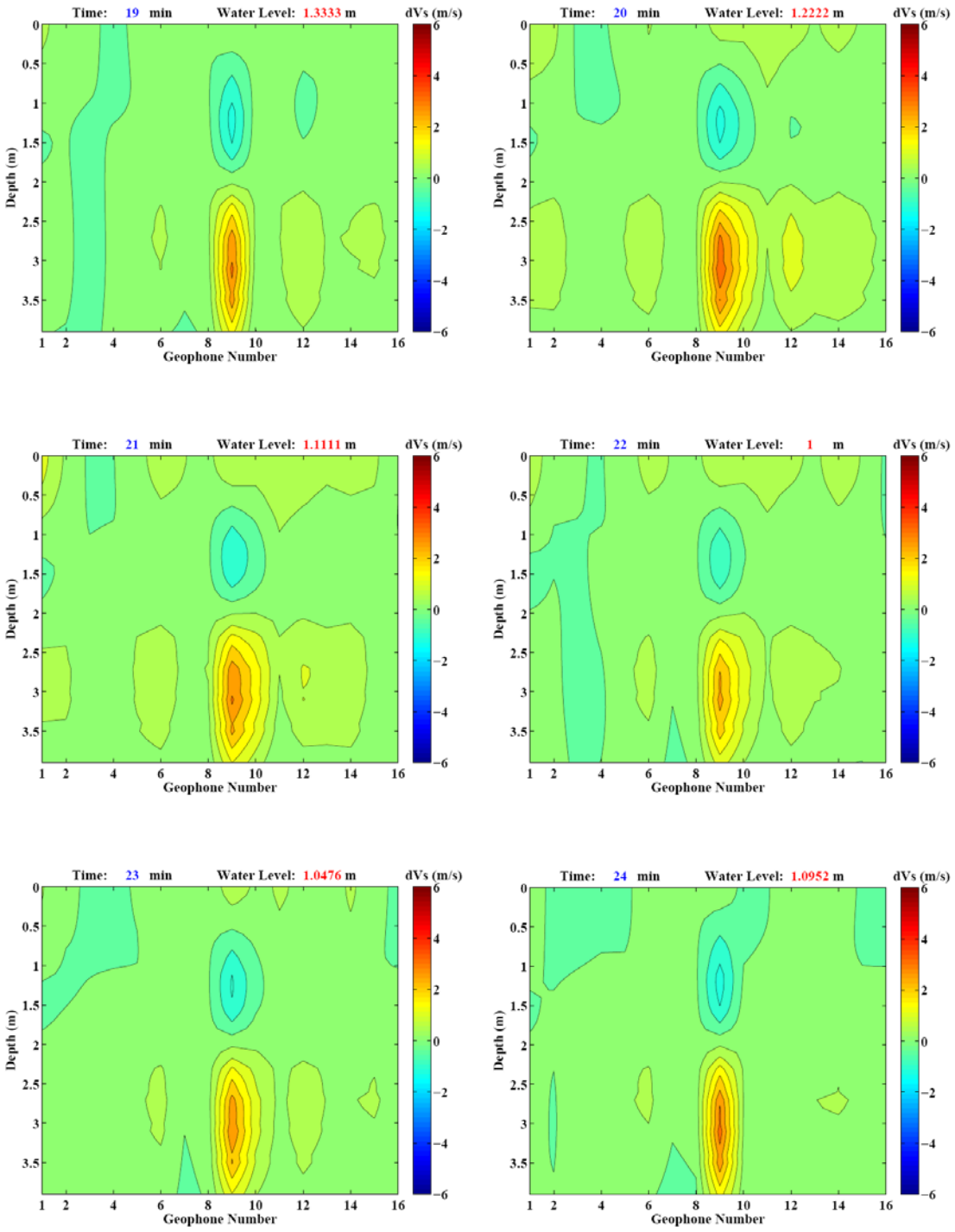

A.1 (continued).

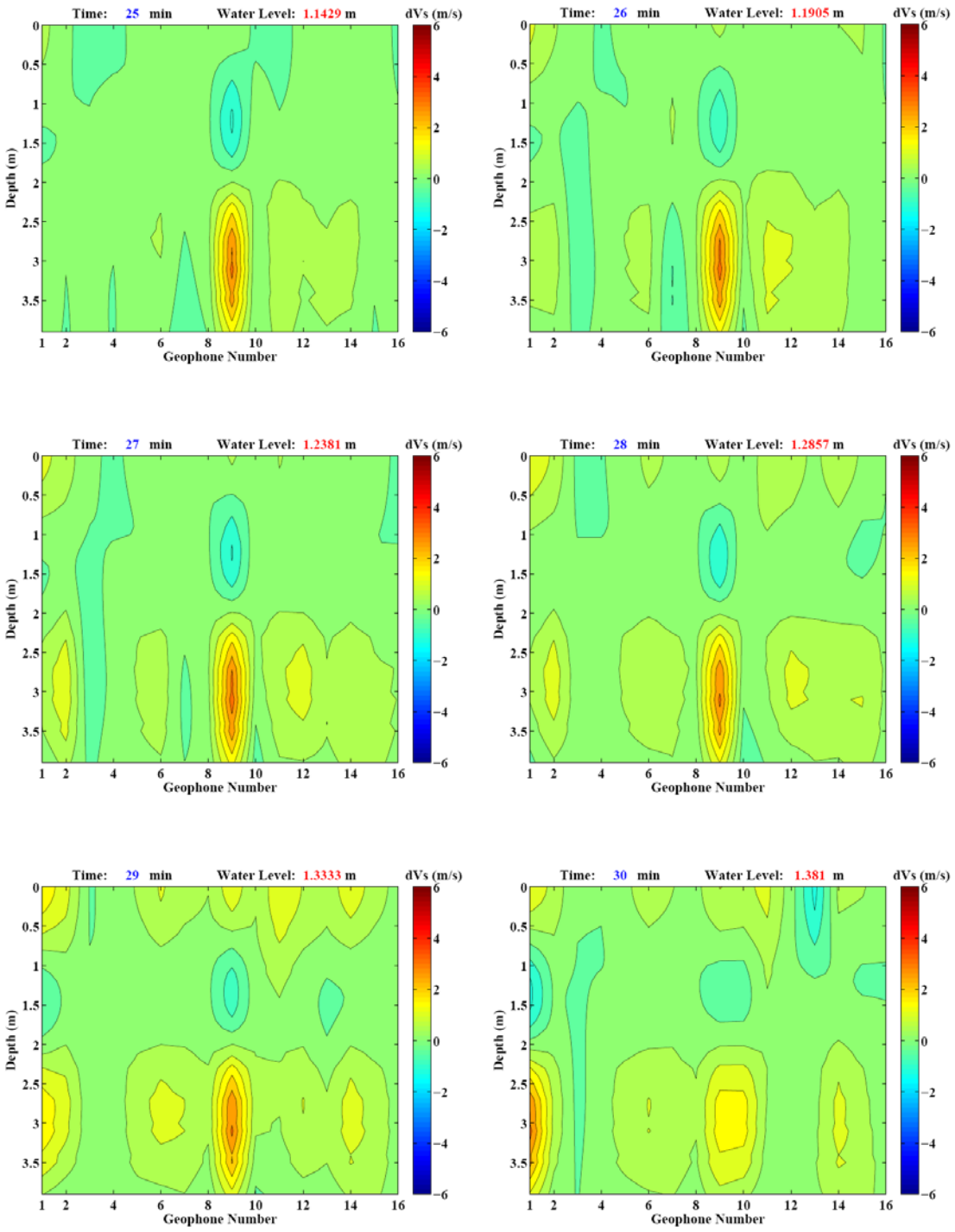

A.1 (continued).

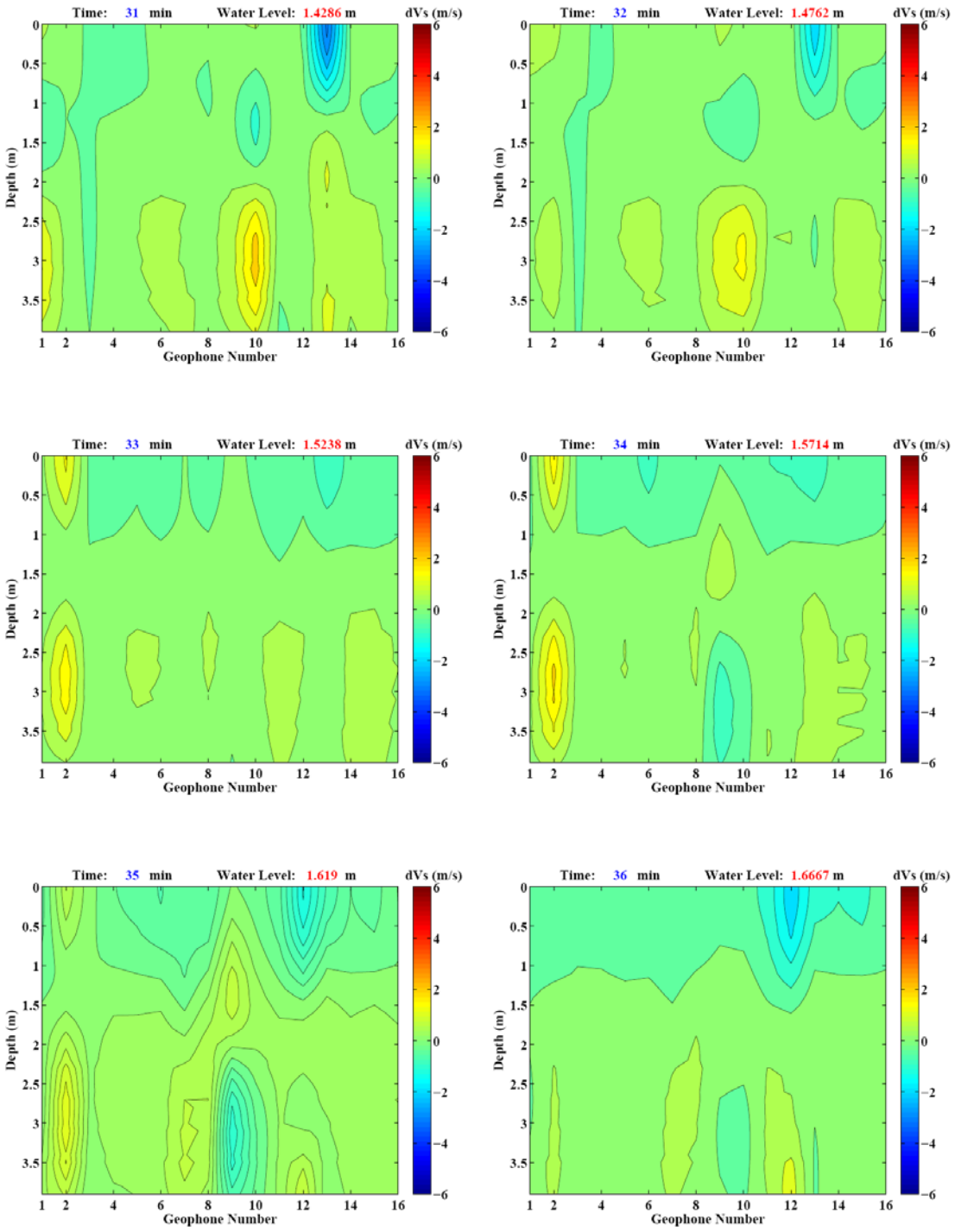

A.1 (continued).

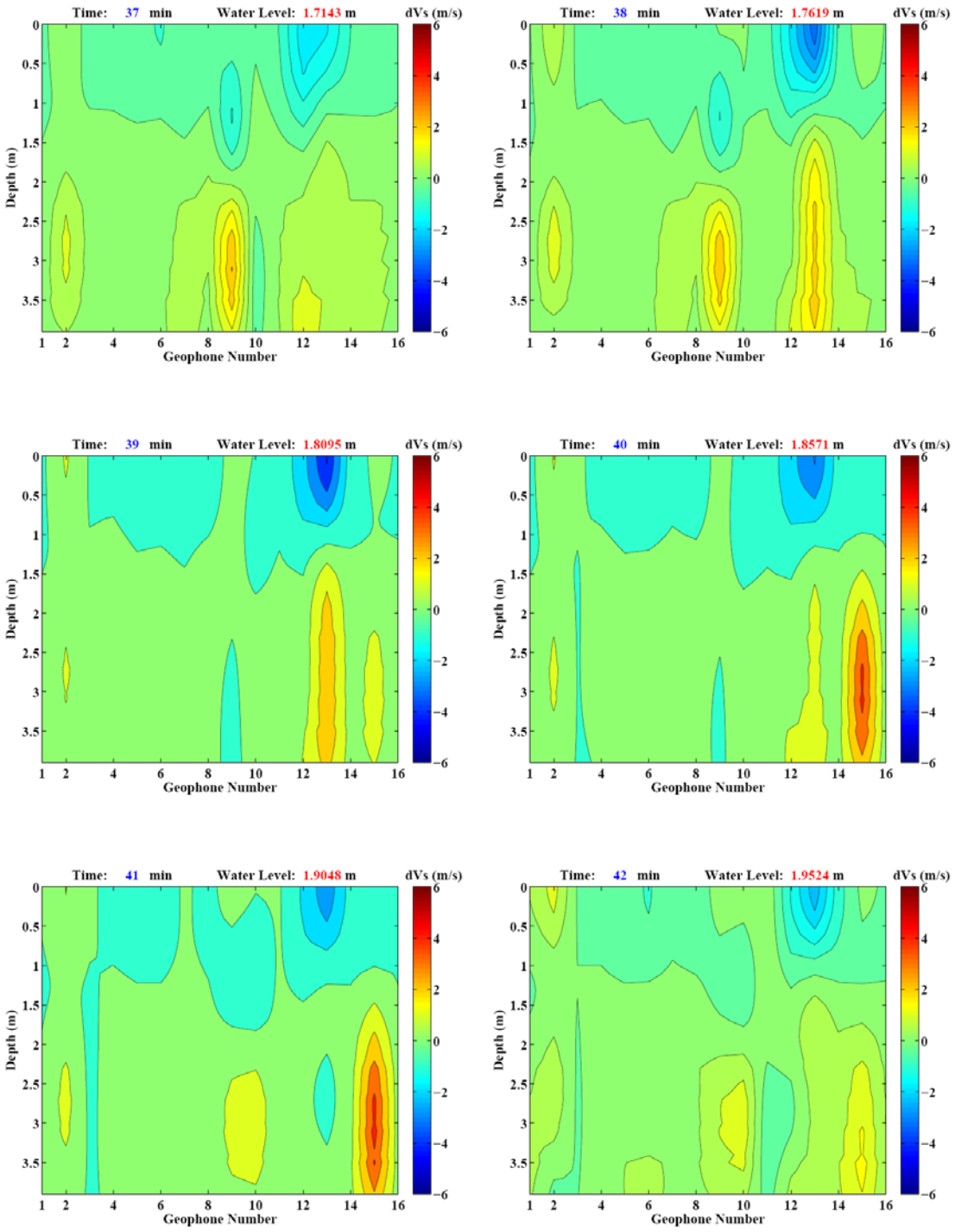

A.1 (continued).

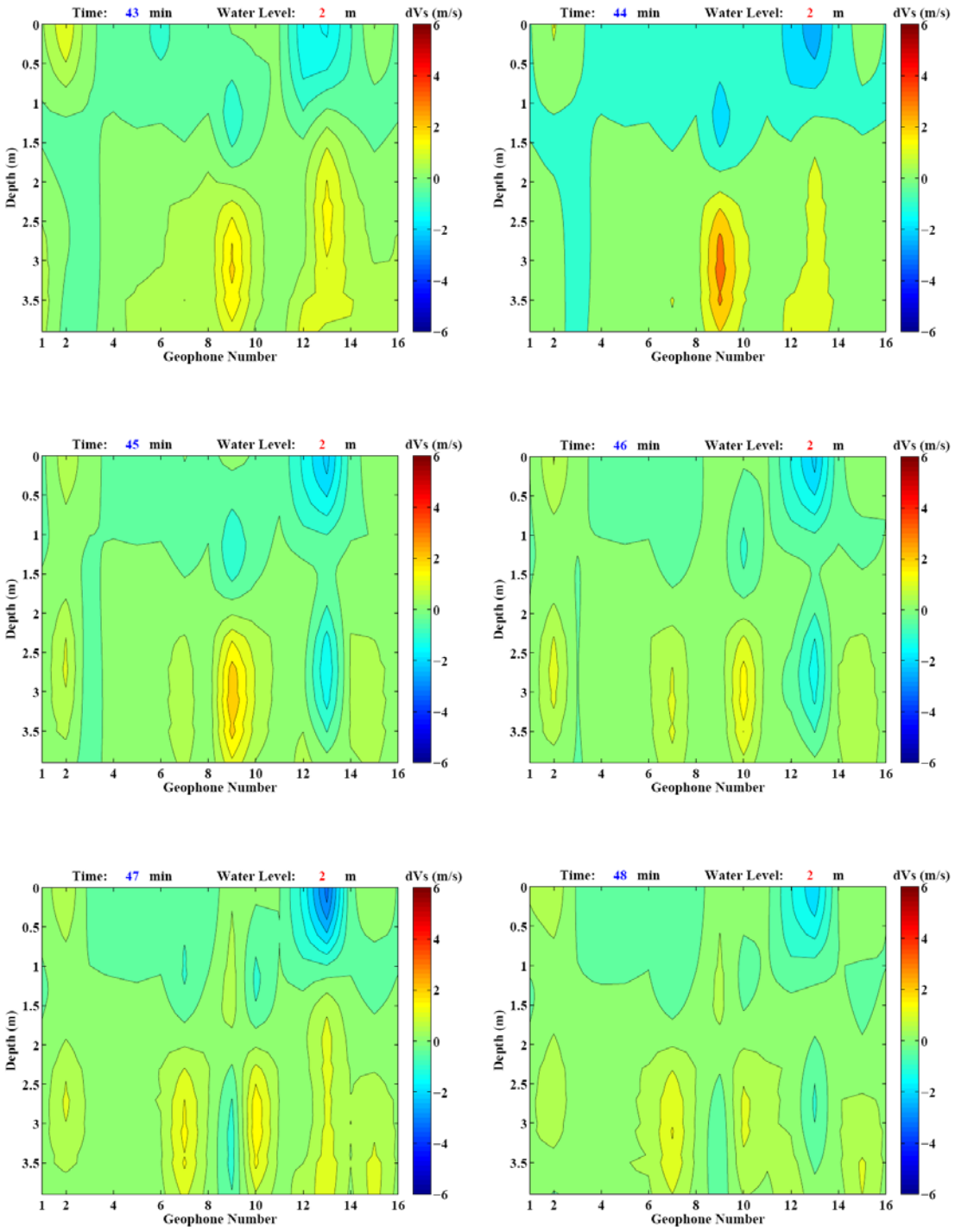

A.1 (continued).

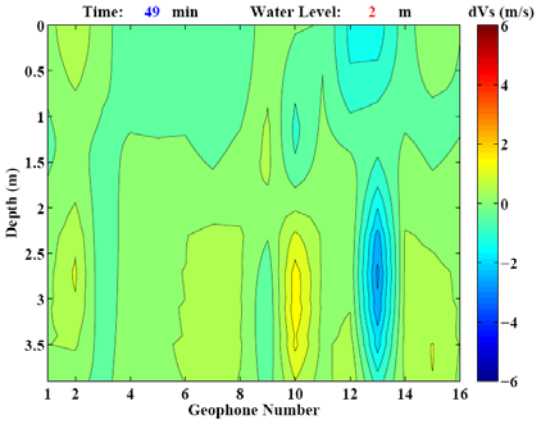

A.1 (continued).

REFERENCES

Abeele, K. E.-A. V. D., J. Carmeliet, P. A. Johnson, and B. Zinszner (2002). Influence of water saturation on the nonlinear elastic mesoscopic response in Earth materials and the implications to the mechanism of nonlinearity. J. Geophys. Res., 107, p. 4-1 - 4-11.

Aguirre, J., and K. Irikura (1997). Nonlinearity, liquefaction, and velocity variation of soft soil layers in Port Island, Kobe, during the Hyogo-ken Nanbu earthquake. Bull. Seism. Soc. Am. 87, 1244-1258.

Archuleta, R. J., S. H. Seale, P. V. Sangas, L. M. Baker, and S. T. Swain (1992). Garner Valley downhole array of accelerometers: instrumentation and preliminary data analysis, Bull. Seism. Soc. Am. 82, 1592-1621.

Aki, K., (1969). Analysis of the seismic coda of local earthquakes as scattered waves, J. Geophys. Res., 74, 3322-3342.

Aki, K., (1988). Local site effect on ground motion, in Earthquake Engineering and Soil Dynamics. II: Recent Advances in Ground–Motion Evaluation, Proc. Of the A.S.C.E. Specialty Conference, 27-30 June, Park City, Utah, J. Lawrence Von Thun (Editor), 103-155.

Aki, K., and K. Irikura (1991). Characterization and mapping of earthquake shaking for seismic zonation, in Proc. 4th Intl. Conf. on Seismic Zonation, Vol. 1, 61-110.

Bachrach, R., and A. Nur (1998). High-resolution shallow-seismic experiments in sand, Part I: Water table, fluid flow, and saturation. Geophys., 63, 1225-1233.

Bachrach, R., J. Dvorkin, and A. Nur (1998). High-resolution shallow-seismic experiments in sand, Part II: Velocities in shallow unconsolidated sand: Geophys., 63, 1234-1240.

Bachrach, R., J. Dvorkin, and A. Nur (2000). Seismic velocities and Poisson's ratio of shallow unsolidated sands. Geophys., 65, 559-564.

Ben-Zion, Y. (1998). Properties of seismic fault zone waves and their utility for imaging low velocity structures, J. Geophys. Res. 103, 12,567-12,585.

Ben-Zion, Y., and C. G. Sammis (2003). Characterization of fault zones. Pure appl. Geophys., 160, 677-715.

Beresnev, I. A., G. M. Atkinson (1998). Stochastic finite-fault modeling of ground motions from the 1994 Northridge, California, earthquake. Bull. Seism. Soc. Am. 88, 1392-1401.

Beresnev, I. A., K.-L. Wen, and Y. T. Yeh (1995a). Nonlinear soil amplification: its corroboration in Taiwan, Bull. Seism. Soc. Am. 85, 496-515.

Beresnev, I. A., K.-L. Wen, and Y. T. Yeh (1995b). Seismological evidence for nonlinear elastic ground behavior during large earthquakes, Soil. Dyn. Earthquake Eng. 14, 103-114.

Beresnev, I. A., K.-L. Wen (1996). Review nonlinear soil response-a reality ? Bull. Seism. Soc. Am. 86, 1964-1978.

Biot, M. A. (1956). Theory of propagation of elastic waves in fluid saturated porous solid. I. Low frequency range. II. Higher frequency range. J. Acoust. Soc. Am., 28, 168-191.

Boore, D. M., L. Seekins, and W. B. Joyner (1989). Peak acceleration from the 17 October 1989 Loma Prieta earthquake, Seism. Res. Lett. 60, 151-166.

Borcherdt, R. D. (1970). Effects of local geology on ground motion near San Francisco Bay, Bull. Seism. Soc. Am. 60, 29-61

Borcherdt, R. D. (1990). Influence of local geology in the San Francisco Bay region, California, on ground motion generated by the Loma Prieta earthquake of October 17, 1989, in Proc. Intl. Symp. Safety and Urban Life and Facilities, Tokyo Inst. Tech., Tokyo, Japan.

Chang, C-Y., C. M. Mok, M. S. Power, Y. K. Tank, H. T. Tang, and J. C. Stepp (1990). Equivalent linear versus nonlinear ground response analyses at Lotung Seismic Experiment Site, in Proc. 4th U.S. Nat'l. Conf. Earthquake Eng., 327-336.

Chin, B.-H., and K. Aki (1991). Simultaneous study of the source, path, and site effects on strong ground motion during the Loma Prieta earthquake: a preliminary result on pervasive nonlinear site effects, Bull. Seism. Soc. Am. 81, 1859-1884.

Darrage, R. B., and A. F. Shakal (1991a). The site response of two rock and soil station pairs to strong and weak ground motion, in Proc. 4th Intl. Conf. Seismic Zonation, Vol. 3, 359-366.

Darragh, R. B., and A. F. Shakel (1991b). The site response of two rock and soil station pairs to strong and weak ground motion, Bull. Seism. Soc. Am. 81, 1885-1899.

Dodge, D., and G. Beroza (1997). Source array analysis of coda waves near the 1989 Loma Prieta, California, main shock: Implications for the mechanism of coseismic velocity changes. J. Geophys. Res., 102, 24,437-24,458.

Field, E. H., P. A. Johnson, I. A. Beresnev, and Y. Zeng (1997). Nonlinear ground-motion amplification by sediments during the 1994 Northridge earthquake, Nature, 390:599-602

Hadley, D. M., and D. V. Helmberger (1980). Simulation of strong ground motions, Bull. Seism. Soc. Am. 70, 617-630.

Hardin, B. O., and V. P. Drnevich (1972a). Shear modulus and damping in soil: measurement and parameter effects, J. Soil Mech. Foundations Div. ASCE 98, 603-624.

Hardin, B. O., and V. P. Drnevich (1972b). Shear modulus and damping in soil: design equations and curves, J. Soil Mech. Foundations Div. ASCE 98, 667-692.

Harmsen, S. C. (1997). Determination of site amplification in the Los Angeles Urban Area from inversion of strong-motion records. Bull. Seism. Soc. Am. 87, 866-887.

Hartzell, S. (1978). Earthquake aftershocks as Green's functions, Geophys. Res. Lett. 5, 1-4.

Higashi, S. and T. Sasatani (2000). Nonlinear site response in Kushiro during the 1994 Hokkaido Toho-oki earthquake. Bull. Seism. Soc. Am. 90, 1082-1095.

Huang, H. C., S. W. Huang, and H. C. Chiu (2005). Observed evolution of linear and nonlinear effects at the Dahan downhole array, Taiwan: analysis of the September 21, 1999 M 7.3 Chi-Chi earthquake sequence. Pure. Appl. Geophys. 162, 1-20, doi 10.1007/s00024-004-2576-4.

Irikura, K. (1983). Semi-empirical estimation of strong ground motions during large earthquakes, Bull. Disaster Prevention Res. Inst., Kyoto Univ. 33, 63-104.

Jarpe, S. P., C. H. Cramer, B. E. Tucker, and A. F. Shakal (1988). A comparison of observations of ground response to weak and strong ground motion at Coalinga, California, Bull. Seism. Soc. Am. 78, 421-435.

Jarpe, S. P., L. J. Hutchings, T. F. Hauk, and A. F. Shakal (1989). Selected strong- and weak-motion data from the Loma Prieta earthquake sequence, Seism. Res. Lett. 60, 167-176.

Jefferson, R. D., D. W. Steeples, R. A. Black, and T. Carr (1998). Effects of soil-moisture content on shallow-seismic data. Geophys., 63, 1357-1362.

Jongmans, D., and M. Campillo (1990). The 1983 Liege earthquake: damage distribution and site effects, Earthquake Spectra, 6, 713-738.

Joyner W., and D. M. Boore (1981). Peak horizontal acceleration and velocity from strong motion records including records from the 1979 Imperial Valley, California, earthquake, Bull. Seism. Soc. Am. 71, 2001-2038.

Kanamori, H., (1979). A semi-empirical approach to prediction of long-period ground motions from great earthquakes, Bull. Seism. Soc. Am. 69, 1654-1670.

Karabulut, H., and M. Bouchon (2007). Spatial variability and non-linearity of strong ground motion near a fault. Geophys. J. Int., doi:10.1111/j.1365-246X.2007.03406.x.

Knight, R., and R. Nolan-Hoeksema. (1990). A laboratory study of the dependence of elastic wave velocities on pore scale fluid distribution. Geophy. Res. Lett. 17, 10, 1529-1532.

Kobayashi, H., and S. Midorikawa (1986). Study of site effects in Mexico City using microtremors, in Proc. Japanese Symp. Earthquake Eng. 7, 355-360.

Li, Y. G., J. E. Steven, S. M. Day, D. D. Oglesby, and E. Cochran (2003). Postseismic fault healing on the rupture zone of the 1999 M 7.1 Hector Mine, California, earthquake. Bull. Seism. Soc. Am. 93, 854-869.

Mayeda, K., S. Koyanagi, and K. Aki (1991). Site amplification from *S*-wave coda in the Long Valley Caldera region, California. Bull. Seism. Soc. Am. 81, 2194-2213.

Mayeda, K., L. Malagnini, and W. R. Walter (2007). A new spectral ratio method using narrow band coda envelopes: Evidence for non-self-similarity in the Hector Mine sequence. Geophy. Res. Lett., 34, L11303, doi: 10.1029/2007GL030041.

Munguia, L., and J. N. Brune (1984). Simulations of strong ground motion for earthquakes in the Mexicali-Imperial Valley, presented at EERI workshop Strong Ground Motion sim.

Murphy, J. R., A. H. Davis, and N. L. Weaver (1971). Amplification of seismic body waves by low-velocity surface layers, Bull. Seism. Soc. Am. 61, 109-146.

Nishimura, T., S. Tanaka, T. Yamawaki, H. Yamamoto, T. Sano, M. Sato, H. Nakamura, N. Uchida, S. Hori, and H. Sato (2005). Temporal changes in seismic velocity of the crust around Iwater volcano, Japan, as inferred from analyses of repeated active seismic experiment data from 1998 to 2003, Earth Planets Space, 57, 491-505.

Ozalaybey, S., M. K. Savage, A. F. Sheehan, J. N. Louie, and J. N. Brune (1997). Shear-wave velocity structure in the northern basin and range province from the combined analysis of receiver functions and surface waves. Bull. Seism. Soc. Am. 87, 183-199.

Pavlenko, O. V., and K. Irikura (2003). Estimation of nonlinear time-dependent soil behavior in strong ground motion based on vertical array data, Pure Appl. Geophys., 160, 2365-2379.

Peng, Z., and Y. Ben-Zion (2004). Systematic analysis of crustal anisotropy along the Karadere-Düzce branch of the North Anatolian Fault, Geophys. J. Int. 159, 253-274, doi: 10.1111/j.1365-246X.2004.02379.x.

Peng, Z., and Y. Ben-Zion (2006). Temporal changes of shallow seismic velocity around the Karadere-Düzce branch of the North Anatolian Fault and strong ground motion, Pure Appl. Geophys., 163, 567-600, doi: 10.1007/s00024-005-0034-6.

Poupinet, G., W. L. Ellsworth, and J. Frechet (1984). Monitoring velocity variations in the crust using earthquake doublets: an application to the Calaveras Fault, California, J. Geophys. Res. 89, 5719-5731.

Relinger, R. E., S. C. McClusky, M. B. Oral, R. W. King, M. N. Toksoz, A. A. Barka, I. Kinik, O. Lenk, and I. Sanli (1997), Global Positioning System measurements of the present day crustal movements in the Arabia-Africa-Eurasia plate collision zone, J. Geophys. Res. 102, 9983-9999.

Rogers, A. M., R. D. Borcherdt, P. A. Covington, and D. M. Perkins (1984). A comparative ground response study near Los Angeles using recordings of Nevada nuclear tests and the 1971 San Fernando earthquake, Bull. Seism. Soc. Am. 74, 1925-1949.

Rogers, A. M., J. C. Tinsley, and R. D. Borcherdt (1985). Predicting relative ground response in Evaluating Earthquake Hazards in the Los Angeles Region, U.S.

Geol. Surv. Profess. Pap. 1360, J. J. Ziony (Editor), 221-248.

Rubinstein, J. L., and G. C. Beroza (2004). Evidence for Widespread Nonlinear Strong Ground Motion in the Mw 6.9 Loma Prieta Earthquake. Bull. Seism. Soc. Am. 94, 1595-1608.

Rubinstein, J. L., N. Uchida, and G. C. Beroza (2007). Seismic velocity reductions caused by the 2003 Tokachi-Oki earthquake. J. Geophys. Res. 112, B05315, doi: 10.1029/2006JB004440.

Sawazaki, K., H. Sato, H. Nakahara, and T. Nishimura (2006). Temporal change in site response caused by earthquake strong motion as revealed from coda spectral ratio measurement. Geophys. Res. Lett., 33, L21303, doi: 10.1029.

Schaff, D. P., and G. C. Beroza (2004). Coseismic and postseismic velocity changes measured by repeating earthquakes. J. Geophys. Res. B: Solid Earth 109, 10, 1-14.

Schneider, J. F. W. J. Silva, and C. Stack (1993). Ground motion model for the 1989 M 6.9 Loma Prieta earthquake including effects of source, path, and site, Earthquake Spectra 9, 251-287.

Seeber, L., J. G. Armbruster, N. Ozer, M. Aktar, S. Baris, D. Okaya, Y. Ben-Zion and E. Field (2000). The 1999 earthquake sequence along the North Anatolia transform at the juncture between the two main ruptures. In the 1999 İzmit and Düzce Earthquakes: Preliminary Results (eds. Barka et al.) (Istanbul Technical University, Turkey 2000) pp. 209-223.

Seed, H. B., and I. M. Idriss (1970). Soil moduli and damping factors for dynamic response analysis, Report EERC 70-10, Earthquake Engineering Research Centre, University of California, Berkeley.

Seed, H. B. (1988). Discussions on nonlinearity, presented at Conf. Earthquake Eng. Soil Dyn. II, Utah.

Singh, S. K., E. Mena, and R. Castro (1988). Some aspects of sources characteristics of the 19 September 1985 Michoacan earthquake and ground motion amplification in the near Mexico City from strong motion data, Bull. Seim. Soc. Am. 78, 451-477.

Takeuchi, H. and M. Saito (1972). Seismic surface waves and earth oscillations. Methods in Computational Physics, 1972, 11: 217-295.

Tanaka, T., S. Yoshizawa, M. Sakaue, and Y. Osawa (1982). Estimation of

acceleration characteristics of strong ground motion by synthesis of accelerogram obtained during a small earthquake, Bull. Earthq. Res. Inst., Tokyo Univ. 57, 561-580.

Tucker, B. E., and J. L. King (1984). Dependence of sediment-filled valley response on the input amplitude and the valley properties, Bull. Seism. Soc. Am. 74, 153-165.

Vidale, J. E., Y. G. Li (2003). Damage to the shallow Landers fault from the nearby Hector Mine earthquake. Nature, 421:524-526.

Wen, K.-L. (1994). Nonlinear soil response in ground motions, Earthquake Eng. Struct. Dyn. 23, 599-608.

Wen, K.-L., I. A. Beresnev, and Y. T. Yeh (1994). Nonlinear soil amplification inferred from downhole strong seismic motion data, Geophys. Res. Lett. 21, 2625-2628.

Wen, K.-L., I. A. Beresnev, and Y. T. Yeh (1995). Investigation of nonlinear site amplification at two downhole strong ground motion arrays in Taiwan, Earthquake Eng. Struct. Dyn. 24, 313-324.

West, M., and W. Menke (2001). Fluid-Induced Changes in Shear Velocity from Surface Waves. Proceedings, Symposium on the Application of Geophysics to Engineering and Environmental Problems (SAGEEP), 21-28.

Yalcinkaya, E. and O. Alptekin (2005). Site effect and its relationship to the intensity and damage observed in the June 27, 1998 Adana-Ceyhan earthquake. Pure Appl. Geophys., 162, 913-930, doi: 10.1007/s00024-004-2648-5.

Yu, G., J. G. Anderson, and R. Siddharthan (1992). On the characteristics of nonlinear soil response. Bull. Seism. Soc. Am., 83, 218-244.

Zinszner, B., P. A. Johnson, and P. N. J. Rasolofosaon (1997), Influence of change in physical state on elastic nonlinear response in rock: Significance of effective pressure and water saturation, J. Geophys. Res., 102, 8105-8120.